NOVEL COLOR-CODED PULSE-BURST MICROSCOPY SYSTEM FOR ULTRA-HIGH SPATIALLY- AND TEMPORALLY-RESOLVED IMAGING OF PRIMARY ATOMIZATION IN ENGINE-RELEVANT DIESEL SPRAYS

A Thesis
Presented to
The Academic Faculty

by

Kenneth F. Maassen

In Partial Fulfillment
of the Requirements for the Degree
Masters of Science in the
George W. Woodruff School of Mechanical Engineering

Georgia Institute of Technology
May 2020

NOVEL COLOR-CODED PULSE-BURST MICROSCOPY SYSTEM FOR ULTRA-HIGH SPATIALLY- AND TEMPORALLY-RESOLVED IMAGING OF PRIMARY ATOMIZATION IN ENGINE-RELEVANT DIESEL SPRAYS

Approved by:

Dr. Caroline Genzale, Advisor
George W. Woodruff School of Mechanical Engineering
Georgia Institute of Technology

Dr. Wenting Sun
George W. Woodruff School of Mechanical Engineering
Georgia Institute of Technology

Dr. Oleksandr Bibik
Daniel Guggenheim School of Aerospace Engineering
Georgia Institute of Technology

Date Approved: January 6, 2020

ACKNOWLEDGEMENTS

I would like to thank my advisor, Dr. Caroline Genzale, for her mentorship of me during this research project. She provided key insight during many of our meetings and guided me through the research process.

Both past and present members of the SPhERe Lab at Georgia Tech have assisted and supported me throughout my two years of research. Dr. Farzad Poursadegh provided significant guidance during my research and introduced me to new optical technology that is instrumental in this work. The help that all other members of the lab provided was so beneficial and allowed me to succeed in this project and get through graduate school.

I wish to thank my father and mother for their constant love and support throughout my life. You nurtured my engineering curiosity from a young age, and I am grateful. I am blessed to have parents that I can always rely on. I dedicate this work to the glory of the Lord, through whom I think, I reason, and I research.

TABLE OF CONTENTS

LIST OF TABLES

LIST OF FIGURES

LIST OF SYMBOLS AND ABBREVIATIONS

AFOV	Angular Field of View [radians]
BEV	Battery Electric Vehicle
CFA	Color Filter Array
D	Diameter of nozzle[m]
D_i	Diameter of droplets in i [m]
ESF	Edge Spread Function
f	Main lens focal length [mm]
f_{img}	Image sampling frequency [um/px]
f_{obj}	Focal length of the objective lens [mm]
FOV	Field of View [μm]
h	Image sensor height [mm]
HCCI	Homogenous Charge Compression Ignition
ICE	Internal Combustion Engine
ISO	International Organization for Standardization
L_{Abbe}	Abbe diffraction resolution limit [μm]
L_{nyq}	Nyquist resolution limit [μm]
LED	Light Emitting Diode
LIF	Laser Induced Fluorescent
LSF	Line Spread Function
M_1	Single lens total magnification [-]
M_2	Two piece lens total magnification [-]
M_{obj}	Microscope objective magnification [-]

MTF	Modulation Transfer Function
NA	Numerical Aperture [-]
n_i	Number of droplets in i [-]
Oh	Ohnesorge number [-]
P_{px}	Pixel pitch on the image sensor [μm]
Re	Reynolds number [-]
SMD	Sauter Mean Diameter [μm]
V	Bernoulli velocity [m/s]
We	Weber number [-]

λ	Wavelength of Light [um]
σ	Surface Tension [N/m]
ρ	Density [kg/m^3]
μ	Viscosity [Pa s]

SUMMARY

Primary atomization, the process of forming droplets from a high-pressure jet, is not a well understood phenomena because it is difficult to study experimentally. Primary atomization occurs on the micron scale over the course of nanoseconds. While numerous experiments have attempted to image primary atomization, they all lack the spatial and temporal resolution to visualize droplet formation. To study droplet formation in primary atomization, a high-performance Color-Coded Pulse-Burst (CCPB) Microscopy system was designed and implemented. This is a novel experimental method for obtaining high-speed (20 Million fps), high-resolution (24MP, 1.2μm resolving power) images. These images are used to study the evolution of fluid structures in an engine-relevant spray and evaluate assumptions in models of primary atomization.

CHAPTER 1. INTRODUCTION

While it is a highly politicized issue, the development of the Internal Combustion Engine (ICE) is crucial for the future of transportation and mobility. Unfortunately, some physics in a modern ICE are not well understood, limiting scientific development. Primary atomization – where droplets are formed from a high-pressure spray - is one of the less understood physical phenomena in an ICE. Current models of primary atomization were developed from macroscopic imaging and scaled sprays, and these have been used to predict and model spray performance throughout the industry. As diagnostic technology has improved, experiments such as ultra-small-angle X-ray scattering have shown that these models fail to predict drop size distribution and liquid mass dispersion in engine-relevant conditions. However, these diagnostics capabilities are limited: since they do not image primary atomization, they provide little suggestions for model improvement.

To this end, a high-performance Color-Coded Pulse-Burst Microscopy imaging system has been developed. The system has framing rates on the order of 10 Million fps, a resolving power of 1.2 μm, and an image resolution of 24 MP. This can image primary atomization in a real diesel spray. Images from this system show ligament breakup and droplet formation on the micron scale of diesel sprays during steady-state flows. These images are then used to critique current models of primary atomization by evaluating underlying assumptions.

CHAPTER 2. BACKGROUND AND LITERATURE REVIEW

2.1 Importance of Internal Combustion and Direct Injection Research

With the ever-increasing threat of climate change, the Internal Combustion Engine (ICE) has found itself in the legislative firing line. In the last decade, technological developments for Battery Electric Vehicles (BEV) have made them an attractive option for consumers because they promise transportation with zero emissions. However, the well-to-wheel impact of BEVs shows that this is far from the truth [1]. While BEVs do not emit on the road, electricity generation and BEV manufacturing cause a significant amount of emissions. Electricity to power the BEVs usually comes from coal, natural gas, or a renewable energy depending on the location. The breakdown of electricity sources for select first world countries is shown in Figure 1 [1]. For BEV's to be net zero, the electricity must come from a renewable source, but often this is not the case. A significant portion of electricity in the EU and USA is generated in coal power plants. Compared to a modern ICE, EVs in regions where coal power plants are dominant emit up to three times more particulate matter per mile [2]. It's not just the BEV that is pitching itself as the transportation solution: Hybrid Electric Vehicles have made similar promises, but these incorporate the ICE.

Hybrids represent an attractive option for the environmentally conscious. Studies have shown that in some cases the well-to-wheel emissions of hybrid vehicles is less than a BEV[3] [4]. This in part comes from less energy required to produce the smaller battery as well as the energy source for charging. Despite what many say, the internal combustion engine has an important role in a net zero world.

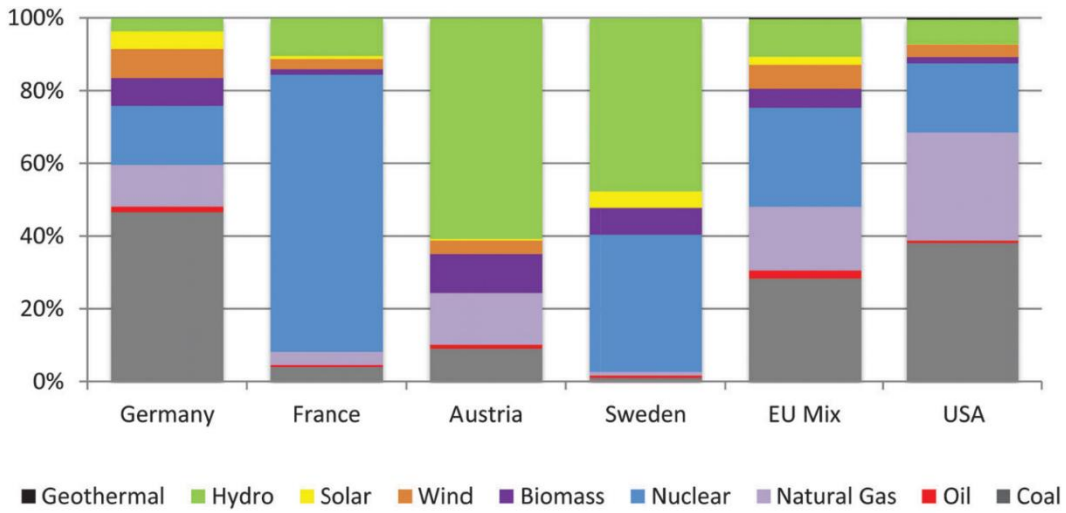

Figure 1: Electricity generation source by country [1].

It's also important to consider the economic aspects of different transportation. The cost of manufacturing a battery is high, and this is reflected in the final cost of the vehicle. This economic driver will continue to push consumers towards the ICE. Recent predictions by Bloomberg, shown in Figure 2, suggest that by 2040 the ICE will occupy 40 percent of the market share for passenger car vehicles [5]. Even the most conservative predictions show that Hybrid and ICE powered vehicles will remain a cornerstone of the transportation industry, so research into ICE development and improvement is needed now more than ever.

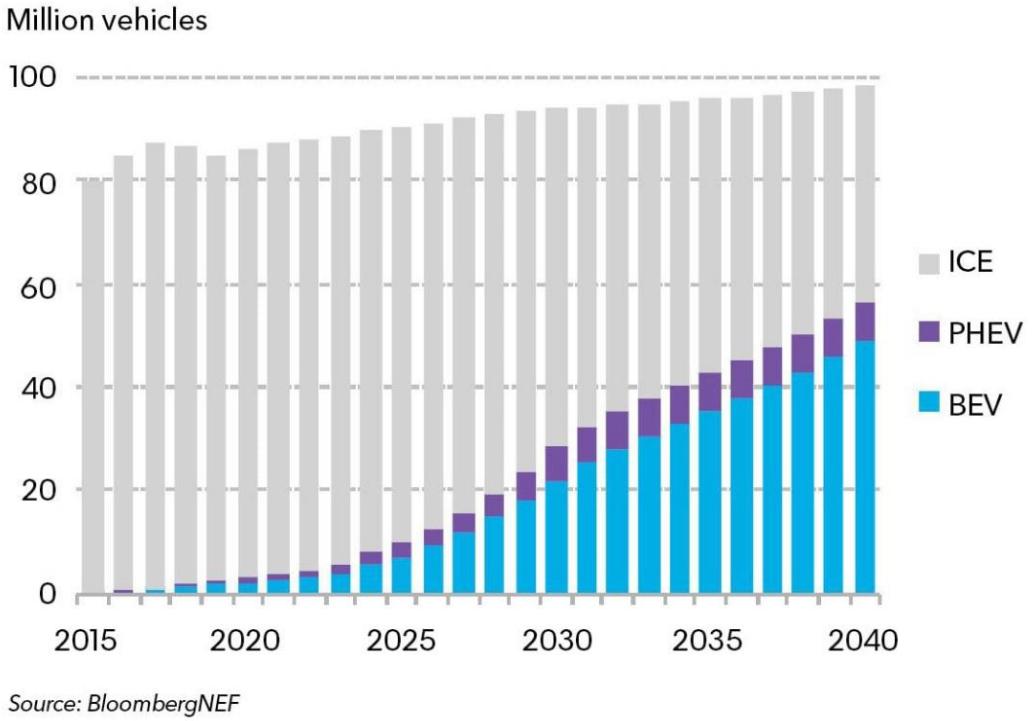

Figure 2: Projected global passenger vehicle sales by drivetrain [5]**.**

Though internal combustion engines have been around for over a century there are still major improvements being investigated. Recent advancements such as variable valve timing (VVT) and the Spark assisted Charge Compression Ignition engine (SPCCI) are two examples [6]. However, many in-engine processes are not well understood and present opportunities for improvement.

A recent advent in engine design, direct-injection allows engineers to have more refined control over the fuel-air preparation for both diesel and gasoline engines. Modern direct-injection systems allow variable injection rates, multiple injections, and multi-fuel combustion. However, the underlying physics of atomization is not well understood therefore injector design is not fully optimized. A better understanding of primary

atomization in fuel sprays could lead to significant advancements in injector design, aiding in reduced emissions.

2.2 Atomization Background

Fuel injection, a high-pressure spray in a high-pressure (up to 100 bar) environment, exhibits a break up mechanism known as atomization. In atomization, a liquid jet evolves into a droplet field in a chaotic and stochastic manner. There are many non-dimensional parameters involved with atomization, and the most common ones are given in Eq. (1) - (4).

$$Re = \frac{\rho V D}{\mu} \tag{1}$$

$$We = \frac{\rho V^2 D}{\sigma} \tag{2}$$

$$Oh = \frac{\sqrt{We}}{Re} = \frac{\mu}{\sqrt{\rho \sigma D}} \tag{3}$$

$$SMD = \frac{\sum n_i D_i^3}{\sum n_i D_i^2} \tag{4}$$

The Reynolds number (Eq. (1)) represents the ratio of internal forces to viscous forces in a fluid and is often used to quantify whether a spray is turbulent. The Weber number (Eq. (2)) is the dimensionless ratio of momentum forces relative to surface tension forces, and the Ohnesorge Number (Eq. (3)) is the dimensionless ratio used to indicate jet stability [7]. The Sauter Mean Diameter (SMD) is the ratio of volume of a fluid to the

surface area of a fluid and is a characteristic diameter for a group of droplets [8]. Atomization models used in CFD simulation of engine combustion typically create correlations with these quantities to determine jet breakup behavior, which are large scale fluid phenomena to describe droplet formation. The four common breakup regimes for a cylindrical jet are shown in Figure 3 [9]. Atomization, the breakup phenomena of interest in this work shown in Figure 3, is where liquid breakup occurs at the nozzle exit of a spray and creates droplets much smaller than the nozzle diameter.

While Rayleigh, First-Wind, and Second-Wind breakup are well understood, atomization is not. This is due to the experimental difficulty in studying the high-pressure microscopic sprays that undergo atomization. As such, current models for atomization were developed from either macroscopic spray images [10] or from scaled sprays [11][12].

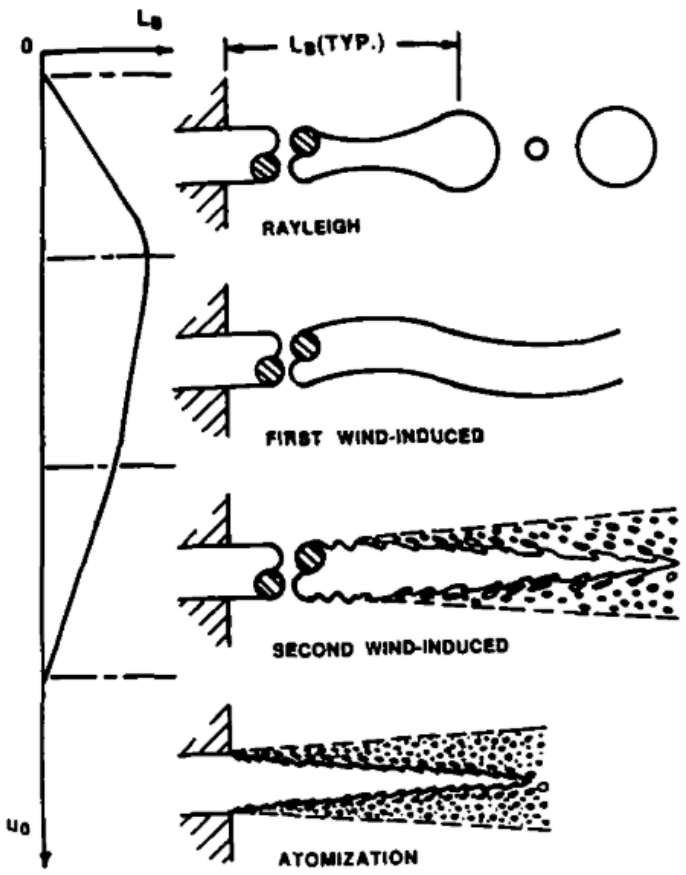

Figure 3: The four major jet breakup regimes as illustrated by Faeth [9]**.**

2.3 State of the Art Models for Primary Atomization

The most widely-adopted atomization model for engine CFD simulations atomization model, the Kelvin-Helmholtz model (K-H) proposed by Reitz et al.[10], theorizes that aerodynamic surface instabilities lead to droplet formation, with drop sizes comparable to the instability wavelength. The underlying idea for the K-H theory is illustrated in Figure 4 [12]. This poses that surface instabilities, developing on the injected liquid jet core, create and shed droplets with diameters on the order of the wavelength of the fastest growing wave and thereby causing a breakup of the intact liquid core. With sufficiently high-resolution and high-speed imaging this assumption is testable.

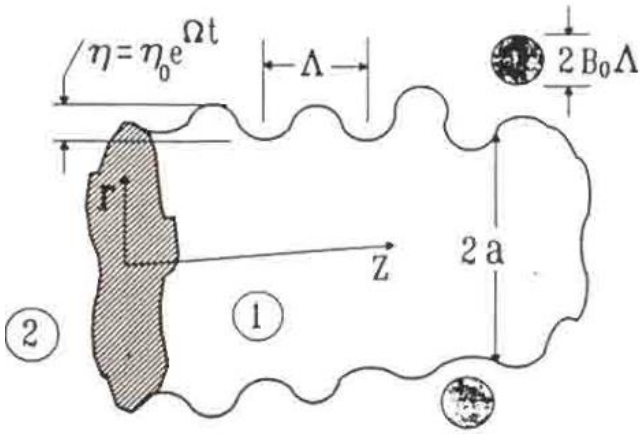

Figure 4: Kelvin-Helmholtz breakup theory as presented by Reitz et al. [12]**.**

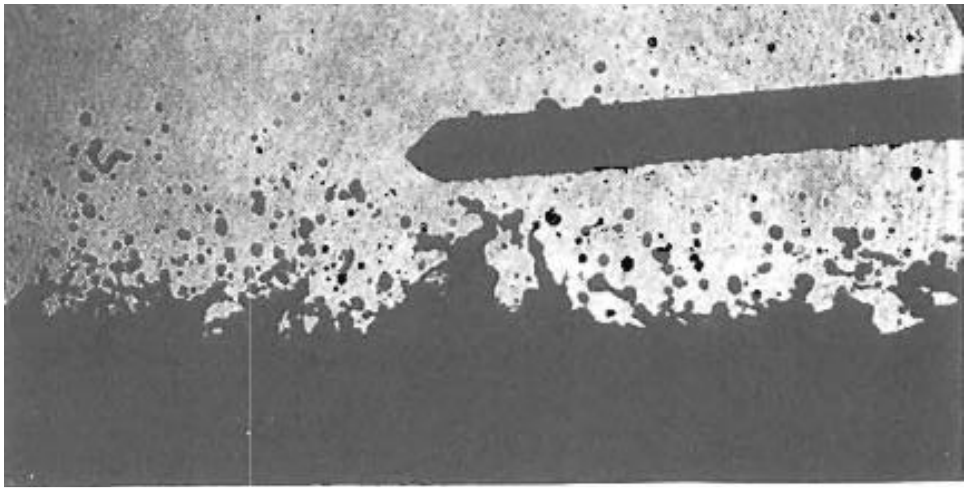

Figure 5: Experimental images of atomization from Wu and Faeth [11]**. Diameter of the reference pin is 0.9 mm and nozzle diameter is 3.6 mm.**

Another significant effort in understanding primary atomization was performed by Wu and Faeth [11]. Unlike Reitz and Bracco, who developed a theoretical model, Wu and Faeth formed empirical SMD correlations by imaging non-dimensionally scaled sprays with nozzle diameters on the order of mm. One image from their work is shown in Figure 5 [11]. Since their models are derived from nozzles with diameters on the order of mm, there are questions to the scalability of their models in real diesel sprays.

Other researchers have modified the K-H model by incorporating other fluid phenomena. One development of the K-H model by Som and Aggarwal introduced cavitation physics [13]. Their model increased accuracy in predicting the projected mass density of a reference data set, but lowered accuracy in predicting spray properties such as the liquid length. Even with a more refined theory, accurate primary atomization models remain elusive.

Many of these atomization models have not stood the test of time. Recent ultra-small angle x-ray scattering experiments disagree with the liquid length and drop size quantities predicted from the K-H model [14]. Improved atomization models are needed to better predict spray performance. For a more accurate atomization model, the features listed in Table 1 need to be imaged and quantified.

Table 1: Features to be imaged to aid in understanding of primary atomization

Features
Droplet Size and Shape
Initial Droplet Formation
Ligament Size and Shape
Surface Instabilities
Intact Liquid Core at Nozzle Exit

2.4 State of the Art Experiments in Primary Atomization

Experimentation on primary atomization is notoriously difficult for the reasons outlined previously. While novel techniques such as Ultra-Small Angle X-Ray Scattering (USAXS) use advanced optical theory to measure droplet size in a spray they fail to see which type of fluid instability forms a droplet [15]. To this end, high performance microscopy has been used to image primary atomization.

New technology like high-speed cameras and high-end scientific lenses have been instrumental in imaging primary atomization. Zaheer used a high-speed camera and a long-distance microscopic lens to visualize droplet formation in a GDI spray at low fuel pressures [16]. Using the high-speed camera, Zaheer was limited to either low framerates or low image resolution.

An attempt to overcome this limit was performed by Kim, where the initial concept of Color-Coded Pulse-Burst Microscopy was used [17]. Kim attempted to use an Infinity K2 long-distance lens and three high-speed pulsed LEDs but found that the Infinity lens exhibited crippling chromatic aberration. His setup has high resolving power, but only captured two useful frames and could not image high pressure sprays due to temporal limit on the LEDs.

Work by Crua et al. used a high speed SIM-16 camera that recorded 16 high-speed frames at 1 Mp resolution, but had a resolution limit of 3 μm with images exposures of 20 ns [18]. These made micron scale features in a steady state spray exhibit significant motion blur, greatly limiting the applicability of their work. Further opportunities to improve this experimental setup certainly exist.

Kirsh and Reddemann used a long distance microscopic lens, custom window, and pulsed Laser based illumination source to achieve an Abbe resolution of 2 μm with 10 ns exposure times [19]. They used a dual frame PIV camera with 1 μs inter frame spacing. These limitations decreased the applicability of their work for analyzing droplets and micron scale ligaments. The high inter frame spacing ensured that temporal information on a single structure was impossible to obtain. Even with the most advanced technology, experimental microscopy is unable to image primary atomization.

While researchers have used single-shot imaging and macroscopic properties to form models of primary atomization, none of these have visualized a droplet being formed from a jet. This is because the length scales (O ~μm) and timescales (O ~ ns) required to image primary atomization presents immense technical challenges. Previous experimental

imaging used off the shelf cameras and lenses, but the resolution limits of high-speed cameras and the temporal limitation of a PIV camera limit the experimental capability for studying primary atomization. A summary of current performance for these researchers is given in Table 2.

Table 2: Performance metric obtained by other state of the art high speed microscopy systems for spray research.

	Exposure	Image Size	Frame Rate	Resolution
Zaheer [16]	20 ns	128 x 48 px	480 kfps	9.8 μm
Kim [17]	33 ns	6000 x 4000 px	1 Mfps	2 – 4 μm
Crua et al. [18]	20 ns	1280 x 960 px	200 Mfps	2.3 μm
Kirsch et al. [19]	10 ns	1024 x 1280 px	1 Mfps	2 μm

2.5 Experimental Requirement for Imaging Primary Atomization

Although there is uncertainty about the droplet formation mechanism in an engine-relevant spray, there is consensus in experimental results that droplet diameters in these sprays are on the order of μm [14][15][20]. The second important parameter in imaging is droplet velocity. For the sake of understanding length and time scales, the Bernoulli velocity of a spray is used for an estimation of flow velocity. The Bernoulli velocity assumes a frictionless nozzle, incompressible flow, and steady state conditions. It is useful for analyzing the order of magnitude of spray velocities. For the fuel used in this work, n-dodecane, the Bernoulli velocity with respect to fuel pressure (injecting into air at STP) is shown in Figure 6. Note that the units in Figure 6 are $\mu m/ns$.

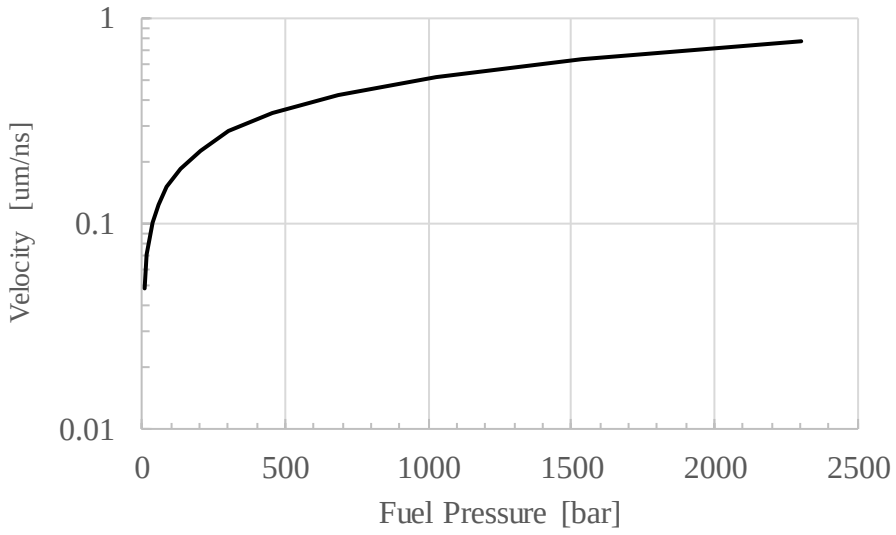

Figure 6: Bernoulli velocity of an n-dodecane spray as a function of fuel pressure, assuming it is injected into ambient air at STP.

The hardest features to image are the fastest and smallest droplets theoretically 1 μm in diameter and travelling at speeds of 600 m/s. To determine inter-frame timing, it must be determined how far the object should move between frames. While a large inter-

frame timing would give a longer time history, it would be more difficult to reliably track the fluid features and droplets. A short inter-frame timing would make features easier to track but would reduce the time history. For illustrative purposes, to reliably track an indistinguishable car in traffic, videos need frames showing the car moving less than a car length. The same is true for microscopic sprays - it is important to capture movement on the scale of an object's size. For objects with diameters between 1 and 10 microns, with velocities between 0.1 and 1 $\mu m/ns$, inter-frame timing will need to be on the order of 10-100 ns. This is equivalent to frame rates of 10-100 Million fps (Mfps).

Another technical challenge in imaging primary atomization is digital image resolution. Digital image resolution sets a limit on the field of view or the magnification of the system in $[\mu m/px]$. For example, on a 1 MP image sensor 1000 pixels wide, a magnification of 0.5 $\mu m/px$ would have a FOV of 500 microns. This limits the information on ligament structure evolution as features will quickly travel out of this FOV. If the magnification is increased to 0.2 $\mu m/px$ to give better reconstructing of droplet diameters, the FOV would be 200 μm and unable to see the full height of a spray. To study primary atomization with μm scale ligaments moving at supersonic velocities, image resolutions on the order of 10 Megapixels are needed. A summary of the performance goals for the diagnostic system is given in Table 3.

Table 3: Diagnostic performance goals to study primary atomization

Metric	Goal
Image Size	> 2000 x 2000 px
Frame Rate	> 10 Mfps
Resolution	< 2 μm
Exposure Time	< 10 ns

CHAPTER 3. DESIGN OF A HIGH-PERFORMANCE COLOR-CODED PULSE-BURST MICROSCOPY IMAGING SYSTEM

3.1 Spectral Microscopy

Color-Coded Pulse-Burst Microscopy, shown in Figure 7, is a concept developed in the SPhERe Lab at Georgia Tech [17]. It overcomes the limits of high-speed cameras and still images by capturing high resolution and high framerate images. Color-Coded Pulse-Burst Microscopy accomplishes this by using a Nikon D5300 color camera and pulsed, temporally color-coded images where the colors align with the detection bands on the Bayer filter. Since the color component of an image is stored with respect to three components (Red, Green, and Blue), three separate images can be stored in the three-color channels and linear algebra can be used to extract the three images. While the concept of color coding images has been implemented in the literature for PIV and low-speed flows [21][22][23], it has not been applied to high-speed, high-resolution microscopy.

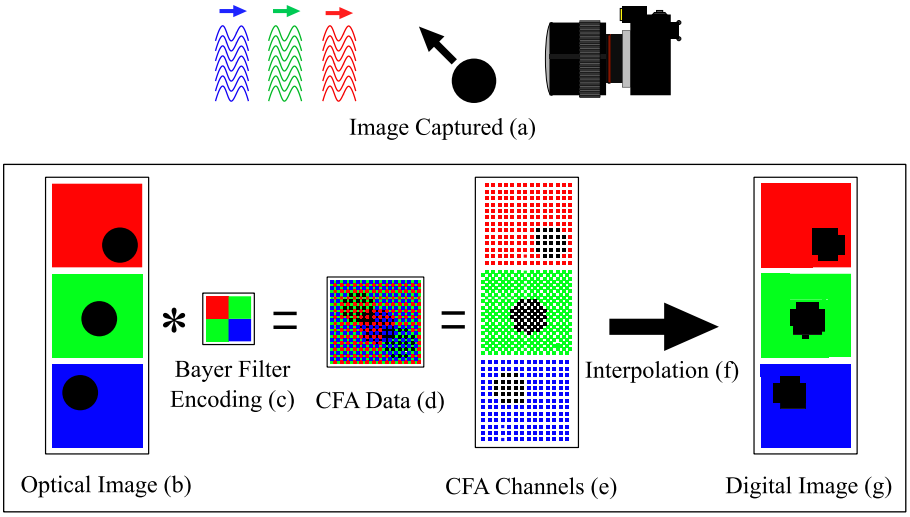

Figure 7: Color-Coded Pulse-Burst Microscopy encodes three frames in a single image file. The optical image (b) is encoded with the Bayer Filter (c) and stored on the Color Filter Array (CFA) (d). The CFA is then demosaiced into three images.

3.2 Optical Design

3.2.1 Optical Background

3.2.1.1 Resolution Limits

The Abbe diffraction limit arises due to diffractions that occur as light waves pass through an aperture. As an image passes through an aperture, the diffraction of rays at that aperture causes a diffraction pattern, transforming an imaged point into a series of bright and dark rings. The image captured by the camera is comprised of airy disks, with diameter of these disks a function of the aperture geometry and light wavelength. This minimum airy disk diameter is the Abbe diffraction limit, given in Eq. (5) [24]. For visible light microscopic application, the wavelength of light is between 400 and 700 μm, and the Numerical Aperture (NA) of the system limits the optical resolving power. The Numerical Aperture of a lens is the ratio of its radius to the distance to the object.

$$L_{Abbe}[\mu m] = \frac{\lambda\ [\mu m]}{2\ NA\ [-]} \tag{5}$$

The other limit of a system's resolving power is the Nyquist limit, defined as twice the sampling frequency ($\mu m/px$) in Eq. (6). While commonly used on 1-D data sets, it also applies to 2-D images. This limit can be changed by increasing the image magnification, but this reduces the incident light per pixel and thereby decreases image quality. There are many tradeoffs when designing an optical imaging system, and it is necessary to define system requirements and constraints.

$$L_{nyq}[\mu m] = 2f_{img}\left[\frac{\mu m}{px}\right] \tag{6}$$

3.2.1.2 Modulation Transfer Function (MTF)

Quantifying the resolving power of an imaging system is necessary to understand its capabilities and limitation. Resolving power goes beyond $\mu m/px$ magnification and includes factors like the quality of lenses and optical limits. While there are multiple methods for quantifying image resolution such as imaging a calibrated chart [25], the most versatile and accepted resolution quantification is the Modulation Transfer Function (MTF) [26]. The MTF analyses a sloped knife edge in an image to quantify resolving power by determining contrast transfer of an image with respect to resolving power in line pairs per millimeter (LPMM). An example of calculating the MTF is given in Figure 8.

There are multiple steps in calculating the MTF. First, an area of a slanted knife edge image is selected as shown in Figure 8 (a). In this example the edge of an etched line-

pair on a slanted USAF target is used. To obtain the edge spread function shown in Figure 8 (b), the perpendicular distance from each pixel to the edge is calculated, and the intensity is plotted with respect to distance from the edge. The line spread function (Figure 8 (c)) is obtained by taking the derivative of the edge spread function and applying a centered hamming window, which isolates the signal from the edge. In Figure 8 (c) the peak in the LSF correlates with the highest slope of the ESF in Figure 8 (b). The MTF shown in Figure 8 (d) is then calculated with a Fast Fourier Transform of the LSF [25]. In order to define a single value of resolution, the 10 percent criteria (10% of the contrast transfer) is used, shown as a dashed line in Figure 8 (d) [26]. In the example shown, the MTF is approximately 600 lpmm, which is equal to $0.83\mu m$. lpmm can be converted to μm by dividing 500 μm by the lpmm measurement. The MTF in this work is calculated using the pre-packaged esfrmat3 code from the ISO standard 12233, and the 10 percent criteria is interpolated in MATLAB [25].

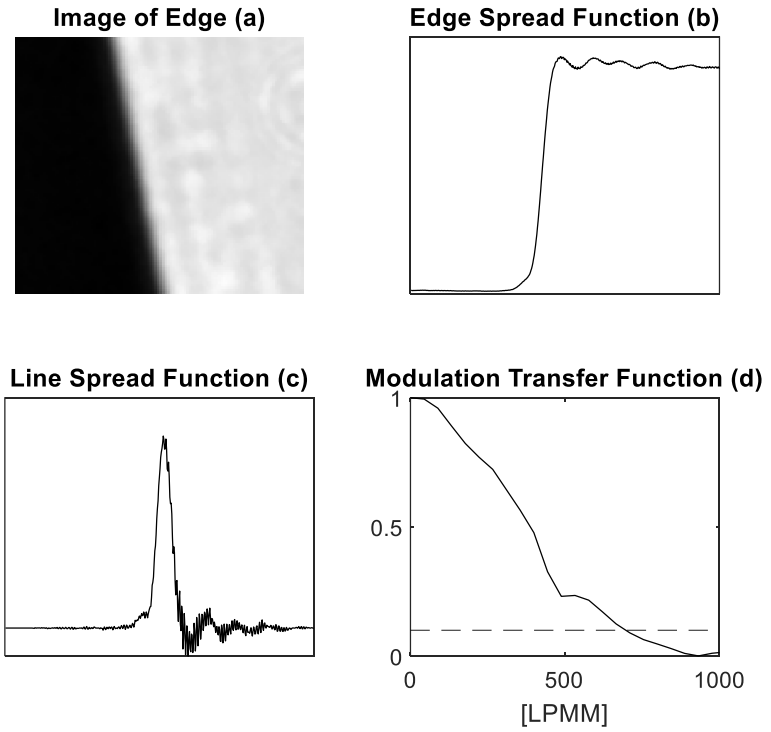

Figure 8: The four steps in computing the Modulation Transfer Function: The original image (a), Edge Spread Function (b), Line Spread Function (c), and the Modulation Transfer Function (d).

3.2.1.3 Camera Gain and ISO

An important camera control that affects image quality is the camera gain, which is known as the ISO for the organization that standardized film sensitivity. The Nikon D5300 used in this work is a consumer grade DSLR with an ISO range from 100 to 25600. Higher ISO helps imaging in darker conditions at the expense of image quality: an image taken at high ISO has a very grainy appearance. To study the effect of ISO on image quality, the average MTF was measured at 30 locations of a USAF test chart while the ISO and shutter speed were varied. The resolution with respect to ISO is shown in Figure 10, with the 95% confidence interval shaded in. It is important to note that the reported value for MTF changed based on location in the test target image up to 5 to 10% of the reported value. This would be a function of either spatially varying resolving power or noise in the image

affecting the MTF calculation. This must be considered for reported MTF values in this paper, as the true value could change up to 5 to 10 % from the reported value depending on location and noise factors.

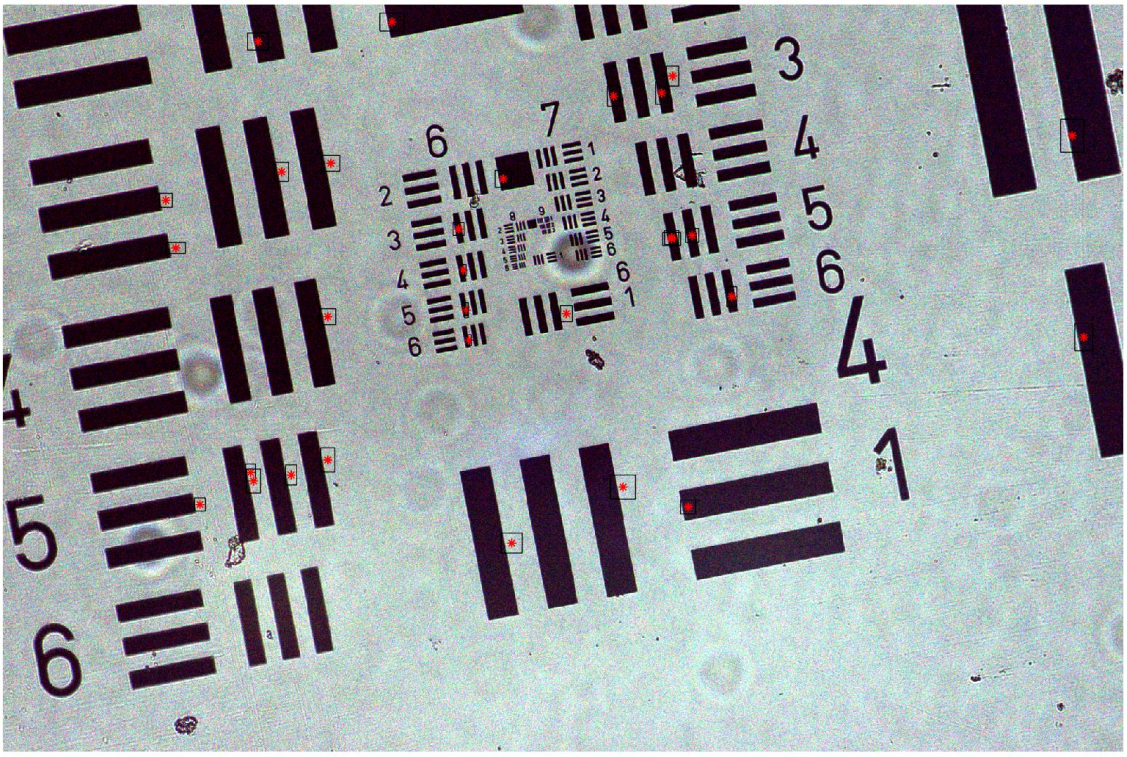

Figure 9: USAF target used for measuring the MTF as a function of ISO. Red stars denote centers of the interrogaiton areas (black rectangles). None of the rectangles interfere with the artifacts from dust, absent in all experimental images.

As ISO increases there is an increase in the average and standard deviation of the MTF, seen in Figure 10. This increased MTF above the Abbe limit and is not possible. One hypothesized cause of this is constructive interference between the noise and the edge. Regardless, images captured above ISO 1000 are unusable as the resolution's

measurements vary significantly and reports values above the Abbe limit of approximately 625 lpmm.

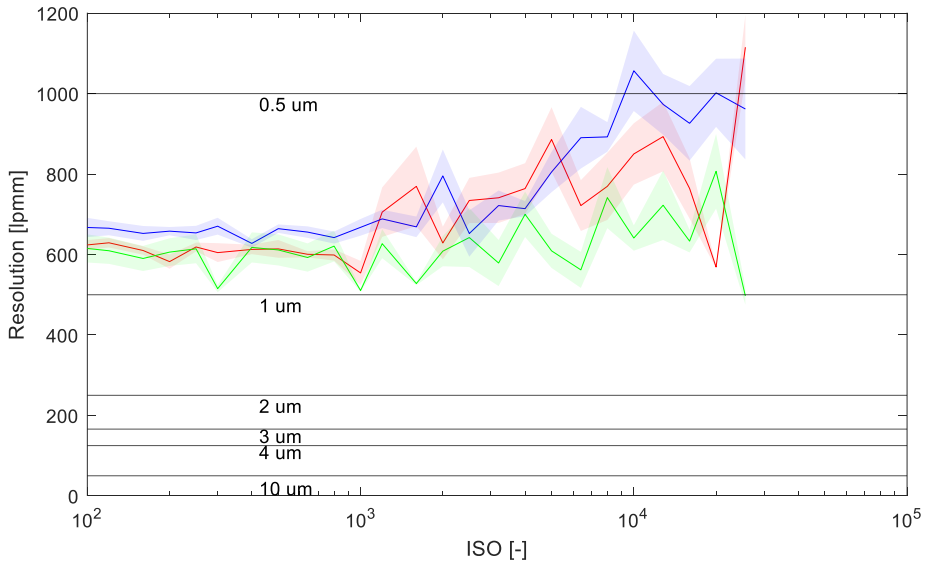

Figure 10: System resolution (MTF) as a function of ISO. The lens (10X+700mm, discussed later) has Abbe limit of 625 lpmm with 450nm light.

To evaluate this assumption, the effect of ISO on the signal to noise ratio (SNR) was measured. As the ISO increased, the SNR of the image decreased. This affected the edge quality and thus the MTF measurement. The average SNR for a row of pixels was calculated for each interrogation region shown in Figure 9 of each image in Figure 10, and is shown in Figure 12 as a function of ISO. In Figure 12 the shaded region represents twice the standard deviation. As SNR decreases, the quality of the MTF measurement decreases because the quality of the derivative approximation for the LSF decreases. MTF plots at these high ISO / low SNR conditions are noisy themselves, so the 10 percent criteria becomes unreliable. Example MTF calculations from a low ISO and high ISO edge are shown in Figure 11 (a) and (b) respectively to show the error when using the 10% criteria. At high ISO, the initial slopes of the MTF curve are consistent with the Abbe limit, but the

10% intercept point and returned MTF value vary significantly due to the noise in the computed MTF curve. This phenomenon is the main reason that MTF measurements increased at high ISO in Figure 10. It is concluded that for this lens (10X+700mm, discussed later) and a properly exposed image with similar backlit illumination characteristics, the maximum camera ISO for scientific images is 1000.

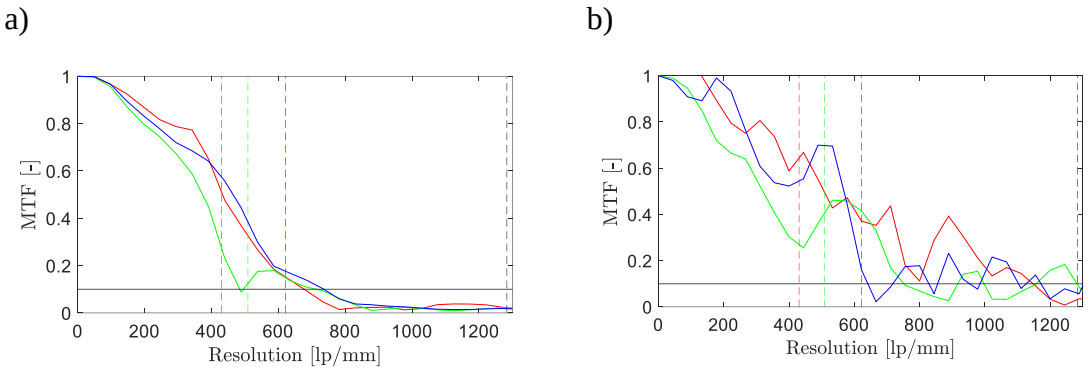

Figure 11: Example of MTF calculation at a) ISO 100 and b) ISO 25600. Colored dashed lines show the Abbe limit, and the 10% criteria is shown with a black line. The lens (10X+700mm, discussed later) has an Abbe limit of 625 lpmm with 450nm light. Images were taken using constant a LED backlight.

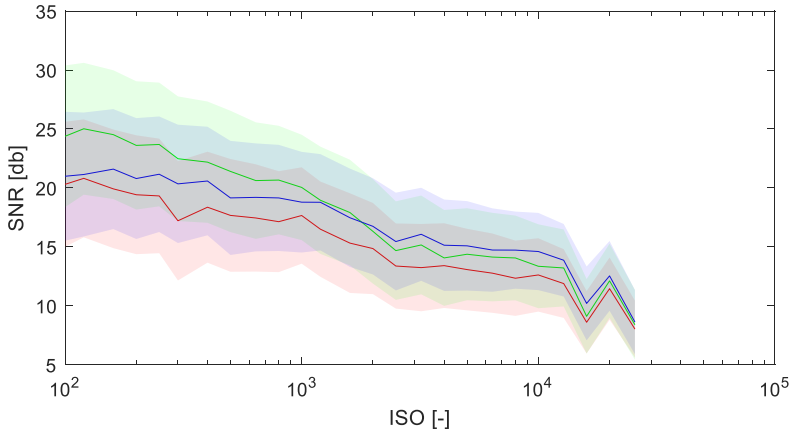

Figure 12: Measured SNR of an image as a function of ISO.

3.2.2 One Piece Lenses for Imaging

In most photography settings, a single camera lens is attached to the camera body. A typical photography lens is 50 - 200 mm focal length. Focal length is directly related to the viewing angle of the lens – the longer the focal length, the narrower the Angular Field of View (AFOV) is. The AFOV is directly related to the camera sensor size (h) and the focal length of the lens (f) in Eq. (7) [27].

$$AFOV = 2\tan^{-1}\left(\frac{h}{2f}\right) \tag{7}$$

Given the AFOV, the effective magnification of a single lens system (M_1) can be solved for by introducing the distance to the object, x_1, in Eq. (8)

$$M_1 = f/x_1 \tag{8}$$

If a 50 mm lens and a 200 mm lens are both used to image an object at a distance of $x_1 = 1\ m$, the image will have higher magnification with the 200 mm lens. This relies on the assumption that both a 50 mm and 200 mm lens have the same minimum focal distance, but the 50 mm focuses closer than the 200 mm lens, so it is not necessarily lower magnification.

Primary atomization of engine relevant sprays occurs on the micron scale, with features moving between 300 and 600 m/s [28]. A microscopic lens is necessary to resolve these features. Most primary atomization imaging utilizes a specially designed long distance microscopic or macro camera lens with extension tubes [17][16][29][30].

Unfortunately, data from these studies is limited, as these lenses have an Abbe diffraction limit of three microns or more – larger than theoretical droplet sizes.

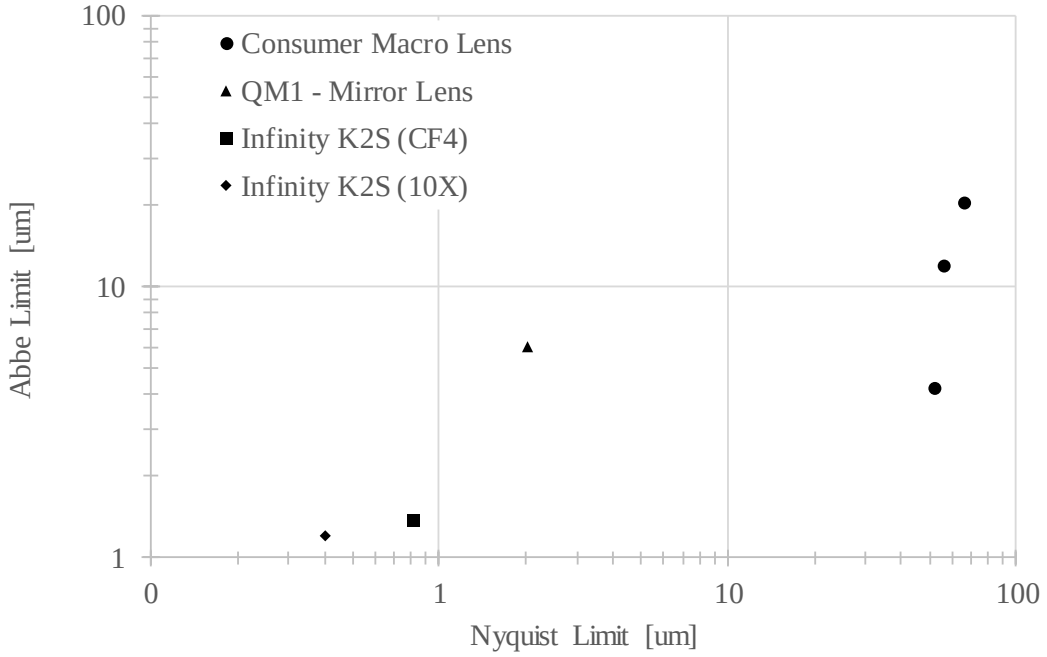

Figure 13: Performance diagram comparing the Abbe and Nyquist limit of standard macro lenses and three microscopic camera lenses.

Two popular long distance microscopic lenses, the Infinity K2S (With CF1B Objective) and Questar QM-100, are diffraction limited to 4 μm amd 6 μm at a working distance of 300mm and 600mm respectively [31][32]. It is possible to use the Infinity K2S with the CF4 or a scientific 10X objective, but this limits the maximum working distance to 50 mm. A comparison for these lenses and other consumer-grade macro lenses used on a Nikon D5300 is shown in Figure 13. All lenses in Figure 13 have either low working distance (they cannot be used outside of the high-pressure chamber and cannot study engine relevant sprays) or are limited to at least 6 μm resolving power. To overcome this limitation, a custom two-piece lens is designed using an objective lens.

3.2.3 Two Piece Lenses for Imaging

A multipiece lens design both lowers working distance and increases resolving power compared to a single lens [19]. This design places an objective lens closer to the object increasing the maximum numerical aperture of the system, decreasing the minimum focusing distance, and improving the system resolving power. The Infinity K2S uses this solution with its objectives.

Due to the optical properties of objective lenses, they are separable from the main lens. This allows them to be mounted remotely inside the spray chamber. Mounting them remotely has a negligible effect on resolving power as the objective lens projects the magnified image to infinity, so the distance between the objective and main lens has a negligible effect. The drawbacks of this design are increased difficulty in lens alignment and an increase in ambient light entering the main lens. These can be overcome with meticulous alignment and turning the lights off in the room, respectively. While it should be easy to use the Infinity K2S lens by separating the objective and main lens, it has been shown to exhibit other problems.

As documented by the SPhERe Lab, severe longitudinal chromatic aberration from the Infinity K2S lens and Infinity objectives makes it irrelevant for Color-Coded Pulse-Burst Microscopy [17]. This aberration prompted a reverse engineering process to understand the function of each optical component in the lens. It was determined that the Infinity lens uses an objective lens (CF-1B, CF4, etc.) a main lens (approximately 700 mm), and lens doublers (NTX tubes). Using a selection of used optical components, a similar lens could be designed for a cost around $1,000; much lower than the approximate

$10,000 cost of an Infinity K2S. While this custom lens would need to be scientifically verified, its theoretical low cost and lack of longitudinal chromatic aberration make it worthwhile to pursue.

3.2.4 Objective Lenses for Magnification

Objective lenses create an image of an object and transmit that image to infinity. When using an objective lens, the distance between the camera sensor and the object imaged, x_1 in Eq. (8), becomes the distance from the camera sensor to the entrance of the main lens. The total system magnification for a two-piece lens, M_2 is given by Eq. (9), where it is also written as a ratio of the focal lengths of the two lenses. In Eq. (9), M_{obj} is the rated magnification of the objective and f_{obj} is the focal length of the objective lens. The Infinity CF4 objective is approximately a 70 mm focal length lens giving an effective 10X magnification with a 700 mm lens.

$$M_2 = \frac{M_{obj} f}{x_1} = \frac{f}{f_{obj}} \tag{9}$$

The two-piece lens design enables the objective and main lenses to be separated. In Figure 14, an objective lens is placed remotely in a high-pressure environment, and it transmits the magnified optical image to the camera lens. The objective lens can withstand higher pressures than the camera, enabling high pressure and high temperature imaging with increased resolving power compared to a single lens system due to its higher Numerical Aperture.

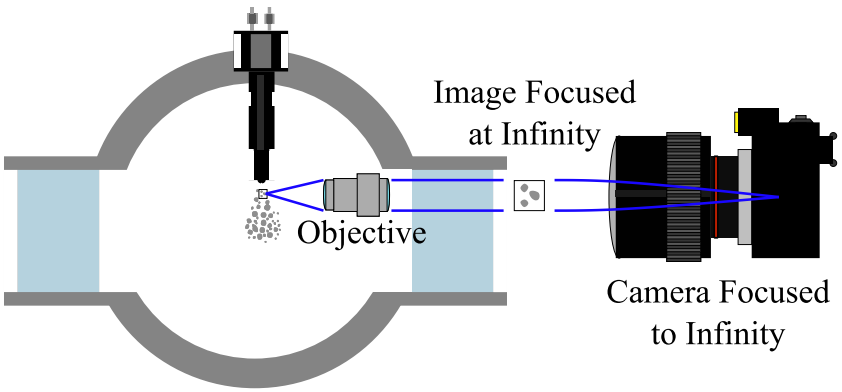

Figure 14: A multi-lens setup for maximum resolution in a high-pressure environment.

3.2.5 Diffraction Limit in a Two-Piece Lens Assembly

A multi-lens assembly places the first lens closer to the object to increase the NA. The effect of the second lens on the diffraction limit is not as straightforward. To explain this, the system is modelled as two separate imaging devices each with an aperture where diffraction occurs (red circles) shown in Figure 15.

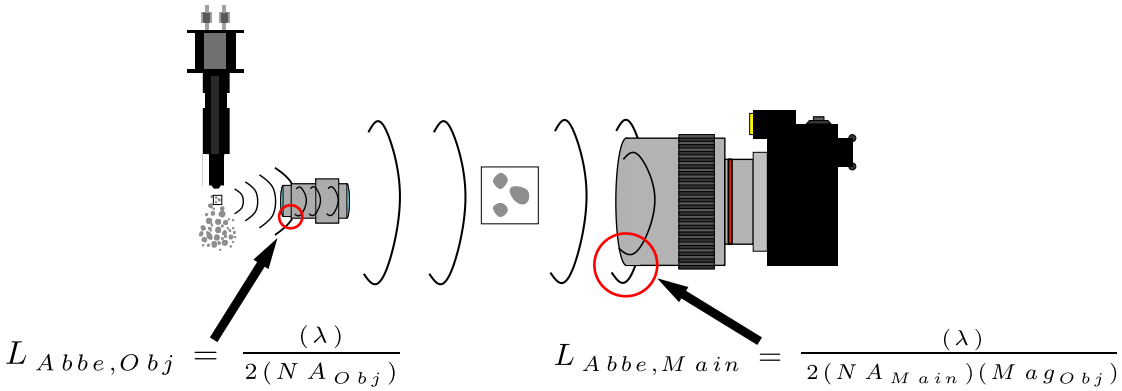

Figure 15: The diffraction from by each component in the Multi-Lens Assembly.

The diffraction limit of the objective lens is only a function of the NA of the objective and the wavelength of light. It is proposed that the diffraction limit for the main lens is calculated the same way, but the diffraction occurs on the magnified image. For an example, a typical 200 mm lens with a 0.1 NA would have a diffraction limit of 3.5 μm at

the intermediate object plane, but since it is viewing a 10X magnified image, the diffraction limit from the 200 mm lens on the imaged object is 0.35 μm. In this example, the objective lens (diffraction limit of 1.2 μm) is the limiting optic.

3.2.6 Total Magnification of a Two-Lens System

The total magnification of the two-piece lens is a function of the objective magnification and the lens focal length. To validate Eq. (9), a relationship was experimentally determined by measuring bars on a USAF target varying main lens focal length. The total magnification of the system as a function of focal length and objective magnification is given in Figure 16.

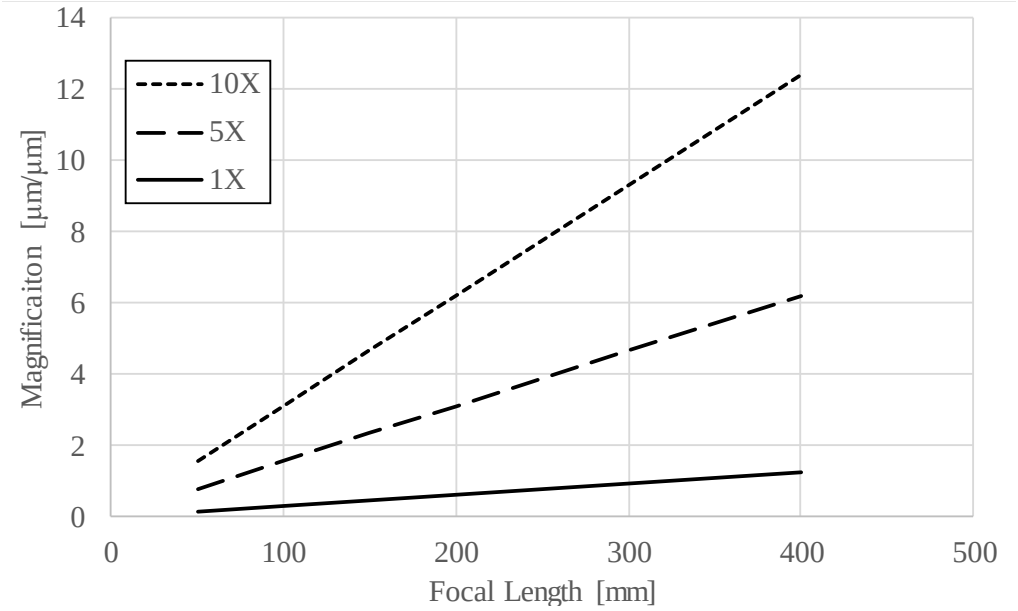

Figure 16: Total system magnification as a function of lens focal length and objective magnification.

Knowing the pixel pitch of the Nikon D5300 (3.89 μm), the Nyquist resolution limit (Eq. (6)) and the Abbe limit (Eq. (5)) can be solved for as a function of lens

configuration. For the Infinity main lens, x_1= 350 mm, and f = 700 mm. The Abbe and Nyquist limits are given in Eq. (10) and Eq. (11) for a two-piece lens design.

$$L_{nyq} = \frac{2P_{px}x_1}{M_{obj}f} = \frac{2P_{px}f_{obj}}{f_1} \tag{10}$$

$$L_{Abbe} = \frac{\lambda}{2\,NA_{obj}} \tag{11}$$

The impact of main lens focal length on the two limits is shown in Figure 17, assuming a constant x_1 of 350 mm. Because of its high NA, the 10X objective has the lowest Abbe limit, and the longer focal length lenses increase the Nyquist limit. For a given objective, there is a point where the two lines intersect. This is where each pixel has the most illumination without theoretical loss of data, however this does not account for 2-d image reconstruction. In reconstructing the airy-disk profile, it is beneficial to have the nyquist limit lower than the Abbe limit, as this gives a better radial reconstruction of droplet diameter from an image using wavelet based algorithms [33].

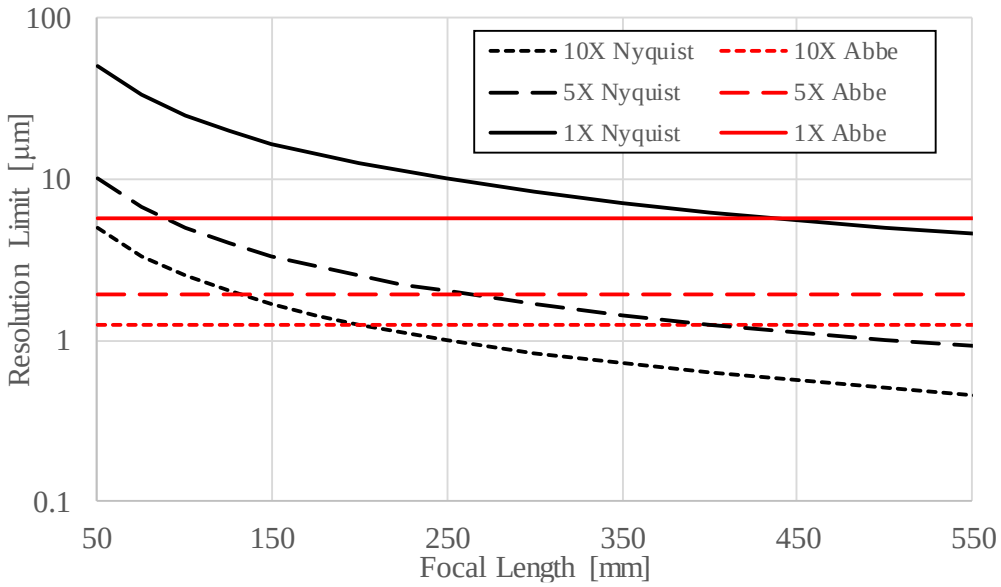

Figure 17: Nyquist and Abbe limits for selected lens and objective combinations.

Based on these calculations and the diagnostic goals outlined in sections 3.2.6 and Table 32.5 respectively, two multi-lens configurations are used in this work. For phase 1, a 5X 0.21 NA objective lens was used in conjunction with an f = 200 mm f/5.6 Nikkor lens (x_1=128 mm) giving a 1.4 μm Abbe limit and a 2.8 μm Nyquist limit. For phase 2, a 700 mm lens (x_1= 350 mm) is used with a 10X 0.28 NA objective, resulting in a 1.2 μm Abbe limit and a 0.4 μm Nyquist limit.

3.3 Extracting Temporal Information from a Color-Coded Pulse-Burst Microscopy Image

3.3.1 Post-Processing Proprietary Nikon Image Files

Most amateur photographers use .JPEG files that cameras record by default, but these files have significant data compression and data loss. While images in this format are compatible with many programs, they undergo a proprietary and undocumented processing algorithm to maximize artistic appeal. This algorithm uses demosaicing and color

correction that inhibits the usability of a Color-Coded Pulse-Burst Microscopy image because it is far from the designed use case. It also causes quality loss and measurement error in the final image, demonstrated in Figure 18, where the MTF from a .JPG image (a) is compared to the MTF from a processed .RAW image (b). In this example, the .RAW image has higher edge quality. The .RAW images files (.NEF proprietary format) must be processed with a custom algorithm to maximize the capability of Color-Coded Pulse-Burst Microscopy.

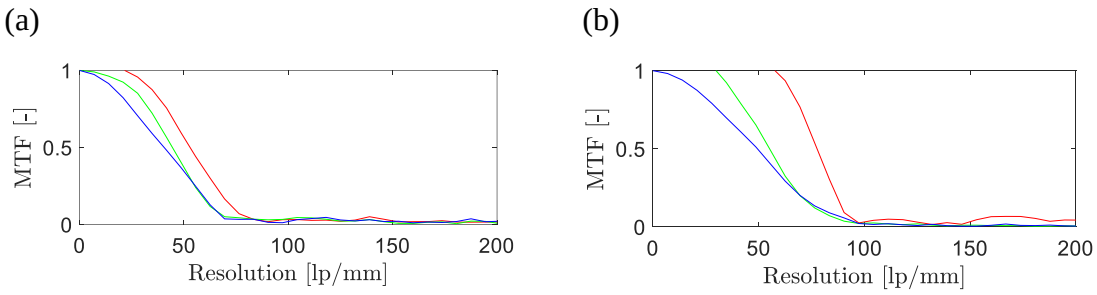

Figure 18: Modulation Transfer Function comparing a .jpg image from the Nikon proprietary algorithm (a) and a post-processed .NEF image file (b).

3.3.2 Correcting for Demosaicing Errors

To process the .RAW images from the camera, the image files were converted from the proprietary Nikon .NEF file type to a more widely used Digital Negative (.DNG) format using a free program from Adobe. The .DNG file was then imported into MATLAB using built in toolboxes [34]. The imported .DNG file contained the CFA data, so three monochromatic images were demosaiced from the CFA as shown in Figure 7 (d). While MATLAB has a built-in demosaicing algorithm, it references the color in other channels during image reconstruction, so a green edge is used to infer a red edge in the red channel. While under traditional color imaging this would improve edge quality, it would degrade edge quality in Color-Coded Pulse-Burst Microscopy [35].

To account for this, a 2D linear-interpolation demosaicing algorithm was created. The pattern that the Bayer filter uses to encode the data on the Nikon CFA is known to be RGGB, shown in Figure 7 (c), so the three channels were easily separated. The empty pixels in each color were then interpolated from their nearest neighbours. The three channels were then overlaid on each other to form a three color image.

One potential drawback of Color-Coded Pulse-Burst Microscopy is that the demosaicing causes images to be ¼ of the resolution of the image sensor, but this can be corrected for by leveraging signals from color cross talk. To use color cross talk to increase image quality, information from all channels and thus all locations is used to reconstruct the image. In fact, color cross talk can enhance image quality in a color coded system for this very reason [36].

3.3.3 Correcting for Color Cross Talk

Designing a Color-Coded Pulse-Burst Microscopy system requires optimizing the spectral sensitives of the camera with the light emission wavelengths to control color cross talk. The Nikon D5300 records color with red, green, and blue filtered pixels, so it is pertinent to use backlights that produce linearly-independent responses from the three different colored pixels. While multiple linearly-independent sets of wavelengths exist that meet this, the simplest approach is to use red, green, and blue light, though some argue that different colors produce higher quality images [36]. To determine the optimum illumination wavelengths a monochromator was used to by Kim to measure the spectral sensitivity of the D5300 image sensor, and this result is replicated in Figure 19 [17]. The spectral sensitivity curves demonstrated that the wavelengths with the least channel cross

talk are 450, 550, and 650nm for red ,green, and blue respectively, which corroborates measured Nikon image sensor spectral sensitivity from the literature [37].

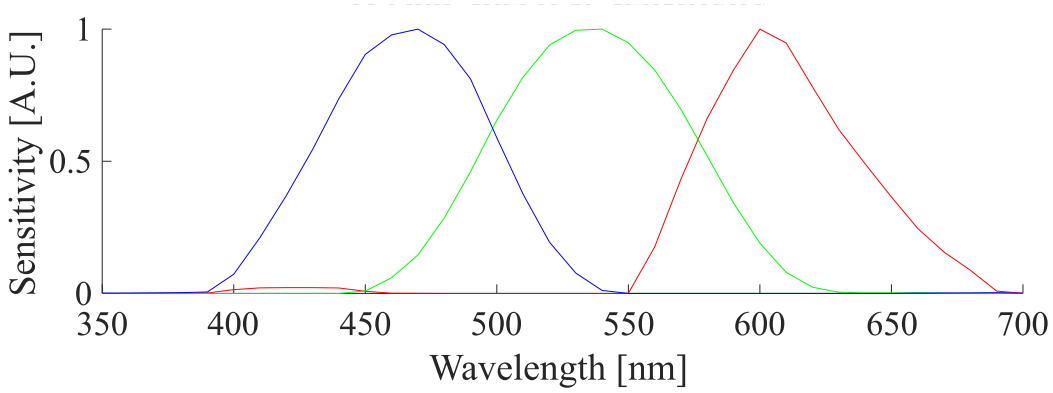

Figure 19: Spectral sensitivity of a Nikon D5300 measured using a monochromator, from Kim (2013) [17]**.**

With the spectral response of the camera quantified, it was necessary to select backlight illumination corresponding to these wavelengths. A laser dye illumination system was chosen, and the spectral emission of the selected dyes is given in Figure 20 [38]. The peak red, green, and blue dye emissions align with the spectral sensitives of the D5300 image sensor.

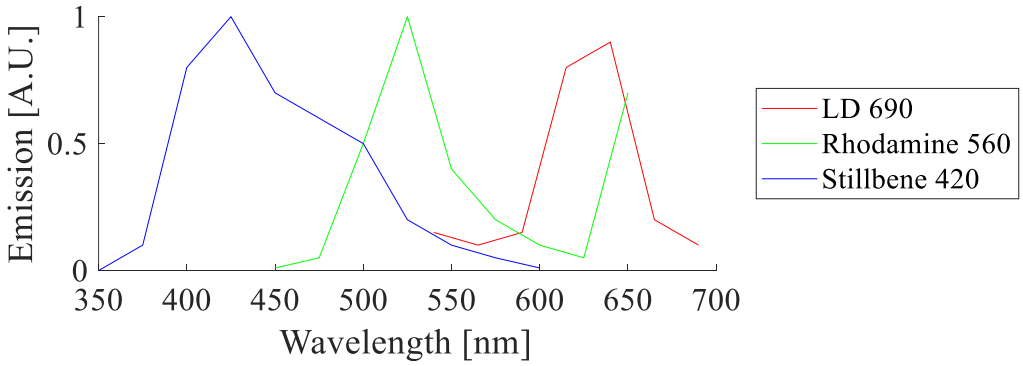

Figure 20: Emission spectra of the designed backlight illumination system [38]**.**

Even with these specially designed backlights the images exhibit color cross talk. To account for this, a calibration was performed. Once the final imaging system was

constructed, Images were taken with a single illumination color and the average red, green, and blue pixel response to each illumination color were measured. The measured values are shown in Figure 21, where the bars represent the normalized response of a pixel or sensor to that backlight wavelength.

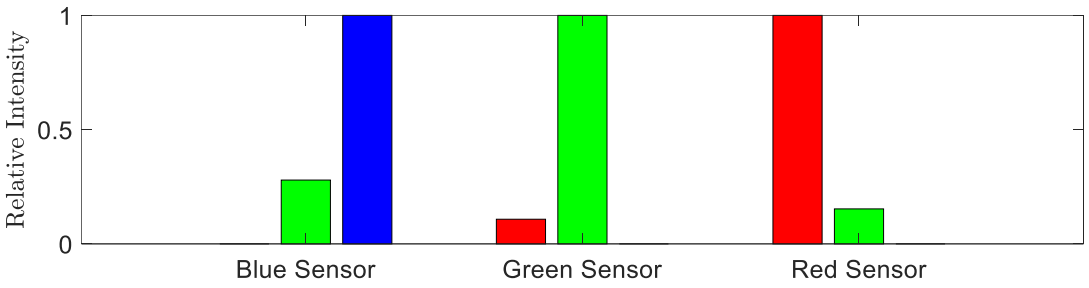

Figure 21: Average red, green, and blue pixel response to the selected illumination wavelengths. In this setup, the green light source excited all pixels.

Linear algebra can be used to correct for color cross talk if the pixels response to the backlight colors is known, [39][40] . The equation for converting the image recorded on the camera (R_C, B_c, G_c, see Figure 7 (e)) to the optical image (R_L, G_L, B_L, see Figure 7 (b)) is given in Eq. (12). In Eq. (12), X_{gr} represents the amount of green light captured on the red pixel relative to the amount of green light captured on the green pixel. For the case shown in Figure 21, $[X_{gr}, X_{gg}, X_{gb}] = [0.2, 1, 0.35]$. In Eq.(12), R_A is the ambient light incident on the red pixel, including both dark-noise and room lighting. Since this system is running at low repetition rates (~ 0.25 Hz) in an ambient environment, the temperature dependence of dark noise is neglected.

$$\begin{bmatrix} R_c \\ G_c \\ B_c \end{bmatrix} = \begin{bmatrix} 1 & X_{rg} & X_{rb} \\ X_{gr} & 1 & X_{gb} \\ X_{br} & X_{bg} & 1 \end{bmatrix} \begin{bmatrix} R_L \\ G_L \\ B_L \end{bmatrix} + \begin{bmatrix} R_A \\ G_A \\ B_A \end{bmatrix} \tag{12}$$

3.4 Tricolor Illumination System Design

The importance and difficulty of photographing microscopic spray ligaments is best appreciated by analyzing spray velocities. For fuel sprays, a reasonable estimation of velocity is the Bernoulli's Equation [16]. High pressure diesel injections occur with fuel pressure on the order of 1000-2000 bar, with fuel density of $700\frac{kg}{m^3}$, into ambient conditions of 10-60 bar. The graph of Bernoulli velocity with respect to fuel pressure is given in Figure 6. For the cases in this study, the spray moves between 300 and 600 m/s, or 0.3 and 0.6 $\mu m/ns$. To freeze a micron scale droplet, a flash duration on the order of ns is required.

3.4.1 Capability of High-Speed LEDs

Used by Kim in early Color-Coded Pulse-Burst Microscopy work, high speed LED drivers such as the LightSpeed HPLS-36 DD18B advertise emitted light pulses less than 100 ns [41]. The response of the HPLS-36 DD18B was measured with a photodiode (Thorlabs DET36A2, 14ns rise time), and found to be 50ns FWHM, shown in Figure 22. With a 50ns FWHM exposure duration, features on a spray injected at 1000 bar would move approximately 25 microns during the exposure which would result in motion blur.

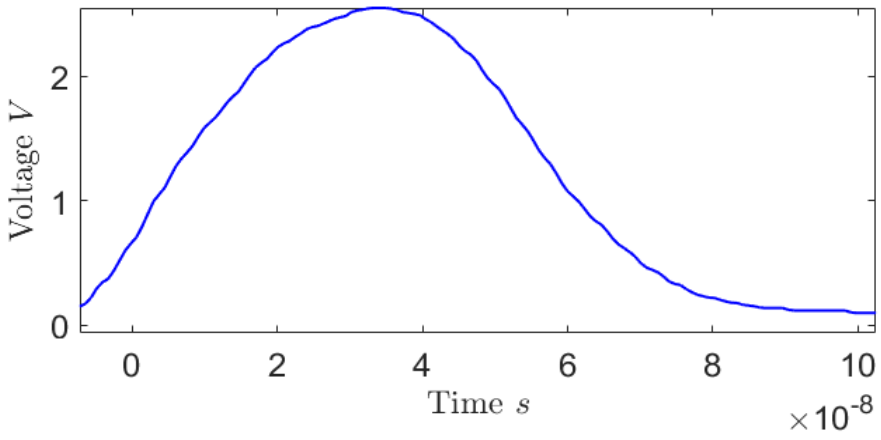

Figure 22: Temporal response of the LightSpeed HPLS-36DD18B.

3.4.2 Laser Induced Fluorescent Illumination

The motion blur obtained from imaging with pulsed LED's on the micron scale does not meet the diagnostic targets outline in Table 3, so a shorter illumination pulse length is necessary. Another solution for illumination is a nanosecond pulsed PIV Laser. These lasers pulse an order of magnitude faster (5 ns instead of 50 ns) than an LED and they have orders of magnitude more power than an LED.

One problem with laser illumination is the speckle effect from beam coherence [42]. To overcome this, Laser-Induced-Fluorescent (LIF) dyes in cuvettes were excited by the Lasers, and these dye cells replaced the LED heads. The dye cells both minimize the speckle effect, by making the subsequent illumination incoherent, and induce a Stokes shift to change the illumination wavelength. A Stokes shift occurs when a particle absorbs the energy in a photon and excites an electron to a higher energy state. The electron then falls to a lower energy state than the ground state and emits a photon with longer wavelength, corresponding to the energy drop. The three LIF dyes were selected so the emitted wavelength would best match the D5300 image sensor sensitivity (see Figure 19 and Figure

20) [38]. A 355 nm laser is used to excite the Stilbene 420 dye which emits light at 450 nm, a 532 nm laser excited the Rhodamine 560 dye which emits light at 560 nm, and a 532 nm laser is used to excite the LD 690 dye which emits light at 650 nm.

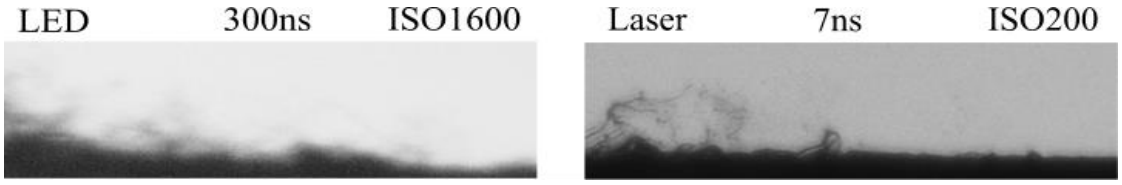

Figure 23: Comparison of the LED backlight and the LASER backlight. Image FOV width is approximately 500 μm. Sprays are from the ECN Spray D injector at 200 bar fuel pressure injecting into air at STP.

The shorter pulse (5 ns) and higher energy (>100 mJ/pulse) of the ND:YAG Laser illumination increased image quality by reducing motion blur and requiring lower camera ISO. A sample image comparing the LIF backlight to the LED backlight is shown in Figure 23, where the top edge of a spray is shown. The image taken with the laser backlight has lower gain and considerably less motion blur. For the 5X + 200 mm lens combination used to image this, the dye emission produced enough illumination for imaging at ISO 200. The LED using a 300 ns pulse required ISO 1600 for enough illumination, which is above the maximum acceptable ISO of 1000 and produces considerable motion blur.

The imaging system for the phase 1 data collection uses unfocused LIF dye illumination and the 5X+200mm lens combination as shown in Figure 24. Color cross talk is minimized by using plate glass filters after the dye cell to match the Bayer filter spectral sensitivity, and spatial illumination variation is controlled with ground plate diffusers after the dye cell. The filters and diffusers are shown in Figure 24. Images from this data set exhibit a few issues: loss of light through the system, lower resolving power, and speckle

effect from lasers passing through the dye cell to the camera. All of these issues are accounted for in the phase 2 system.

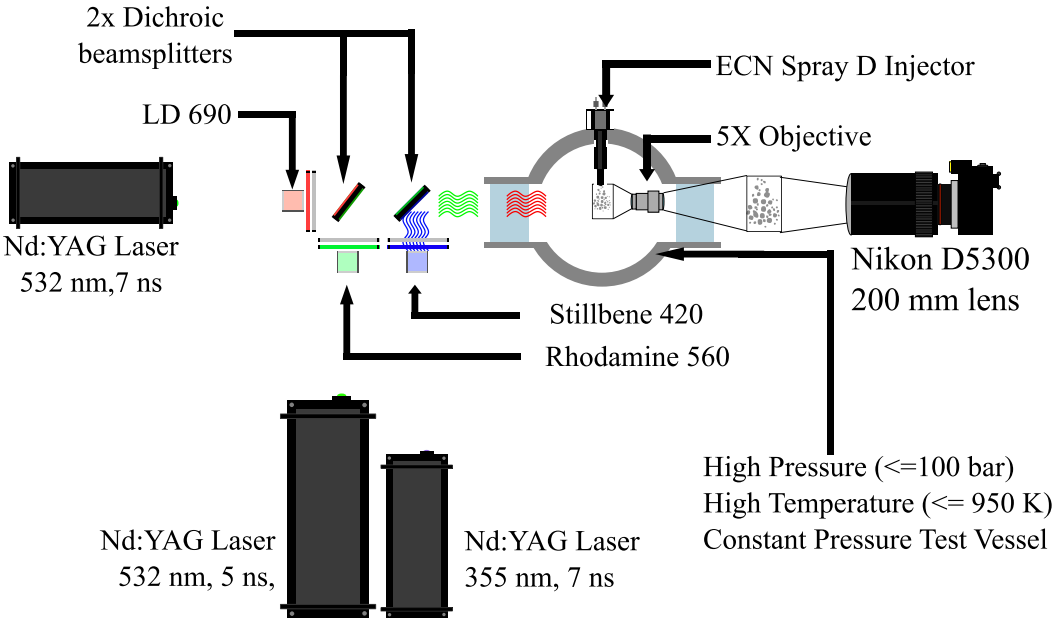

Figure 24: Experimental setup used for phase 1 data collection, with unfocused LIF illumination and a 5X + 200mm lens combination

3.4.3 Focused LIF Illumination System

While the LIF illumination works well with magnifications of 1.4 $\mu m/px$, higher magnifications of 0.2 $\mu m/px$ (10X + 700mm lens) require higher light flux to capture the same number of photons per pixel. Based on pixel area alone, the magnification increase reduces light per pixel by a factor of 49. An image taken with the 5X+200 mm lens at ISO 600 would need ISO (600*49) or ISO 29400 if imaged with the 10X+700 mm lens combination. This is above the camera's maximum ISO of 25600 and far above the acceptable criteria of ISO 1000. To image at the higher magnification, an optical solution is required to optimize the light throughput. This is done using collecting and focusing

lenses in the LIF setup, shown in Figure 25. For the setup used in the experiment, the red and green light used a 2” diameter f = 32 mm lens for focusing, and the green light used a 2” diameter f = 50 mm lens. Captured light was transmitted through the 1” dichroic mirrors and focused to the image area using a 2” diameter f = 50 mm lens. This focusing system increased illumination by a factor of 32, allowing fully exposed images at ISO 800 with the 10X+700 mm lens combination.

To address the residual speckle effect, the phase 2 lighting system incorporated spatial filtering of the laser beams. This is shown with the UV laser path in Figure 25, where the laser is at an oblique angle to the lens so light from the laser is not directly transmitted to the camera. By combining these improvements with the 10X+700 mm lens combination, the system is capable of imaging at 0.2 $\mu m/px$ with 5 ns exposures at ISO 800.

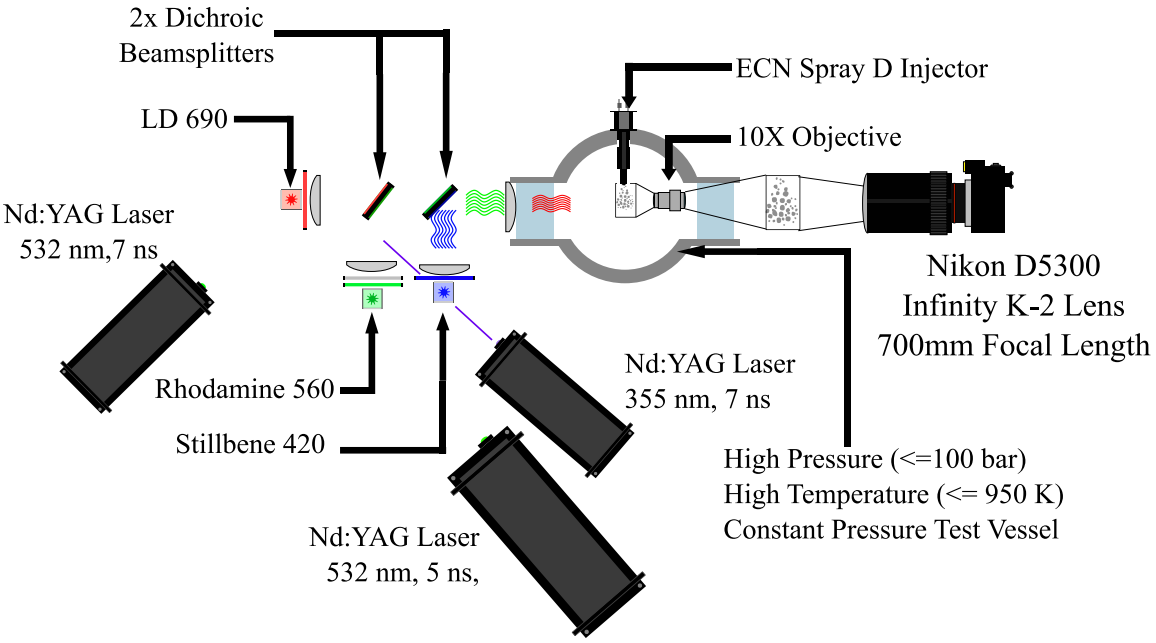

Figure 25: The phase 2 Color-Coded Pulse-Burst Microscopy imaging system. The lenses in the light train capture the emitted light from the dye cell and focus the light to the image area. The oblique positioning of the lasers spatially filters the laser beam from the dye cell light.

3.4.4 Multicolor Illumination Equalization and Power Control

One challenge with a tricolor system is equalizing the illumination of the colors. The D5300 uses one dynamic range per image, so intensity had to be comparable in the three colors. This was accomplished with multiple power controls: the power level on the laser, diffusers, and Q-switch timing. An incremental process was performed to equalize the exposures. Coarse controls (placing diffusers to reduce light and adjusting power settings on the lasers) were done first, and fine controls (q switch timing) were adjusted next. The laser exciting the green dye had the highest power, so it was run on the lowest power with a diffuser between the dye cell and the mirror (Figure 25) and a longer focal length collecting lens (narrower light collection angle). The laser exciting the blue dye was the least powerful, so the red and green LIF output was tuned to match its illumination power.

3.5 Imaging System Performance

3.5.1 Resolution Chart Images

To demonstrate system resolving power, images of a USAF target were taken with both the 5X+200 mm lens and the 10X+700 mm lens. The image taken with the 5X+200 mm lens and a 560 nm backlight is shown in Figure 26, and the image taken with the 10X + 700 mm lens and a 450 nm backlight is shown in Figure 27. Note the scaling of group 6, 7, 8, and 9 for ease of readability in Figure 27 as compared to Figure 26. The smallest bars resolvable with the 5X+200 mm lens (group 7, element 1) are 3.9 μm wide. With the 10X+700 mm lens, the smallest resolvable bars are last two elements in group 8, corresponding to line widths of 1.2 and 1.1 μm.

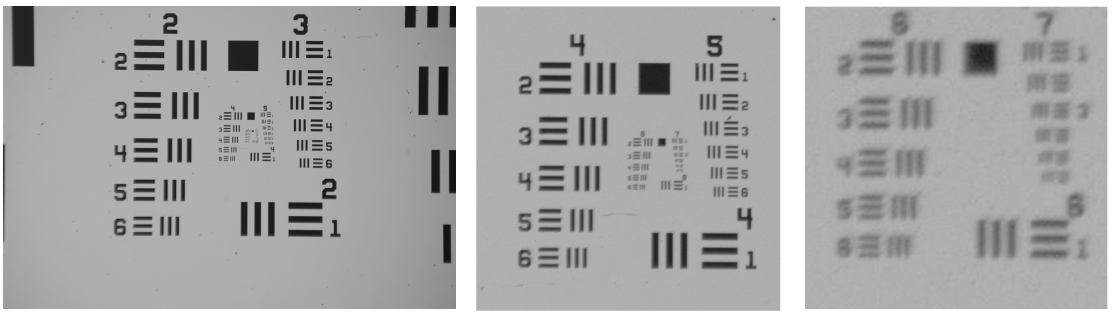

Figure 26: Image of a USAF target taken with the 5X objective and f = 200 mm Nikkor lens with a 450 nm backlight. All images are cropped from full frame photo (left) and scaled for visibility.

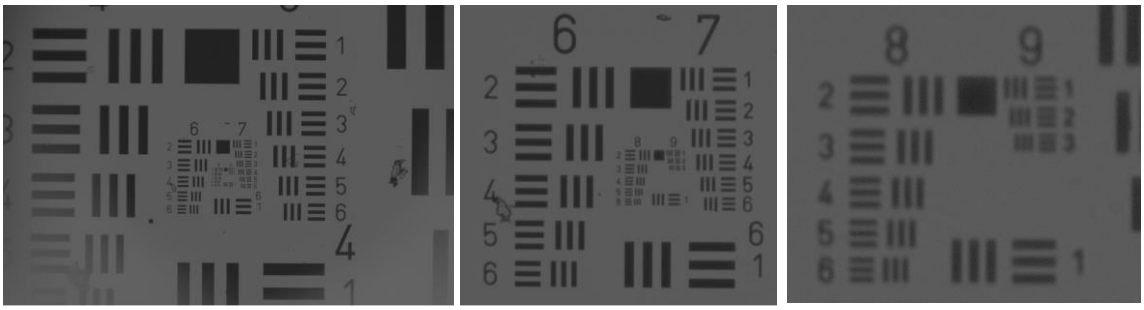

Figure 27: Image of USAF test chart with the 10X objective and infinity K2S 700 mm lens. All images are cropped from full frame photo (left) and scaled for visibility.

The 5X+200 mm lens used during phase 1 to demonstrate the initial concept of a multipiece lens and was later refined with the 10X+700 mm combination in phase 2. The images taken in phase 1 with the 5X+200 mm lens and unfocused LIF illumination still contain useful information, and larger features within the resolving power of the system in these images are analyzed.

3.5.2 Effective Frame Rate

Consistent image timing is necessary for scientifically relevant temporal information. To measure inter-frame timing, a Thorlabs DET36A photodiode with a 50 Ohm shunt resistor was used, which had a 14ns rise time. Triggering the Lasers using the built-in q-switch timing made inter-frame spacing repeatable to approximately 300 ns (~ 3 Million fps). Controlling both the lamp and q-switch from a Berkeley Nucleonics model 575 controller made the inter-frame spacing repeatable to approximately 1ns. With this setup, 300 ns inter-frame spacing was used for phase 1 imaging and 75ns inter-frame spacing (~ 13 Million fps) was used for phase 2 imaging. This timing change was performed because the higher magnification needs higher frame rates to track fluid features. The measured

timing for the phase 1 system is shown in Figure 28, and the measure timing for the phase 2 system is shown in Figure 29.

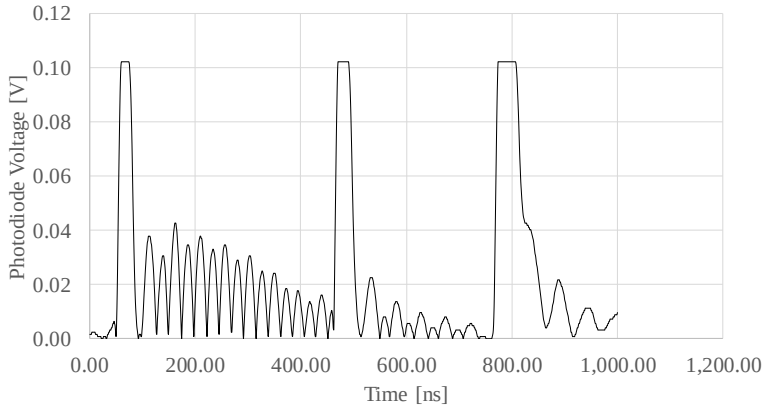

Figure 28: Phase 1 illumination timing recorded with a Thorlabs DET36A photodiode (14ns rise time)

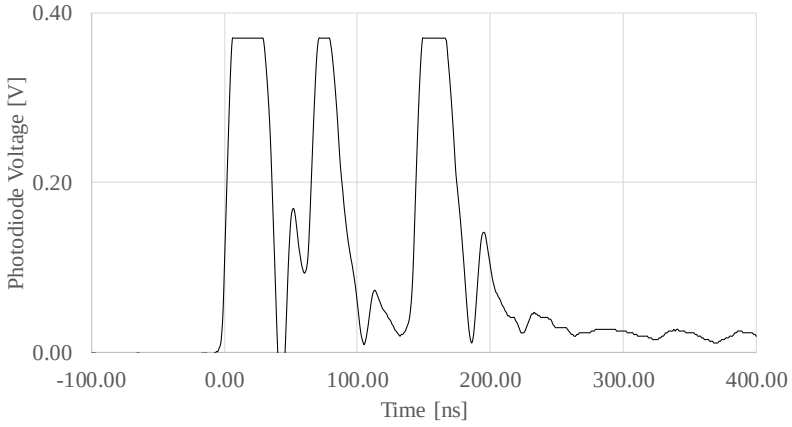

Figure 29: Phase 2 illumination timing recorded with a Thorlabs DET36A photodiode (14ns rise time)

3.5.3 Optical Resolving Power

The MTF for the both phase 1 and phase 2 systems is compared to the system used by Zaheer (Figure 30 (a))[16], shown in Figure 30 (b) and (c). The QM-1 has a limit around 75 LPMM which is equivalent to 7 μm, the phase 1 system has a resolution of

approximately 130 LPMM or 3.8 μm, and the phase 2 system has a resolution of approximately 500 LPMM, or 1.0 μm.

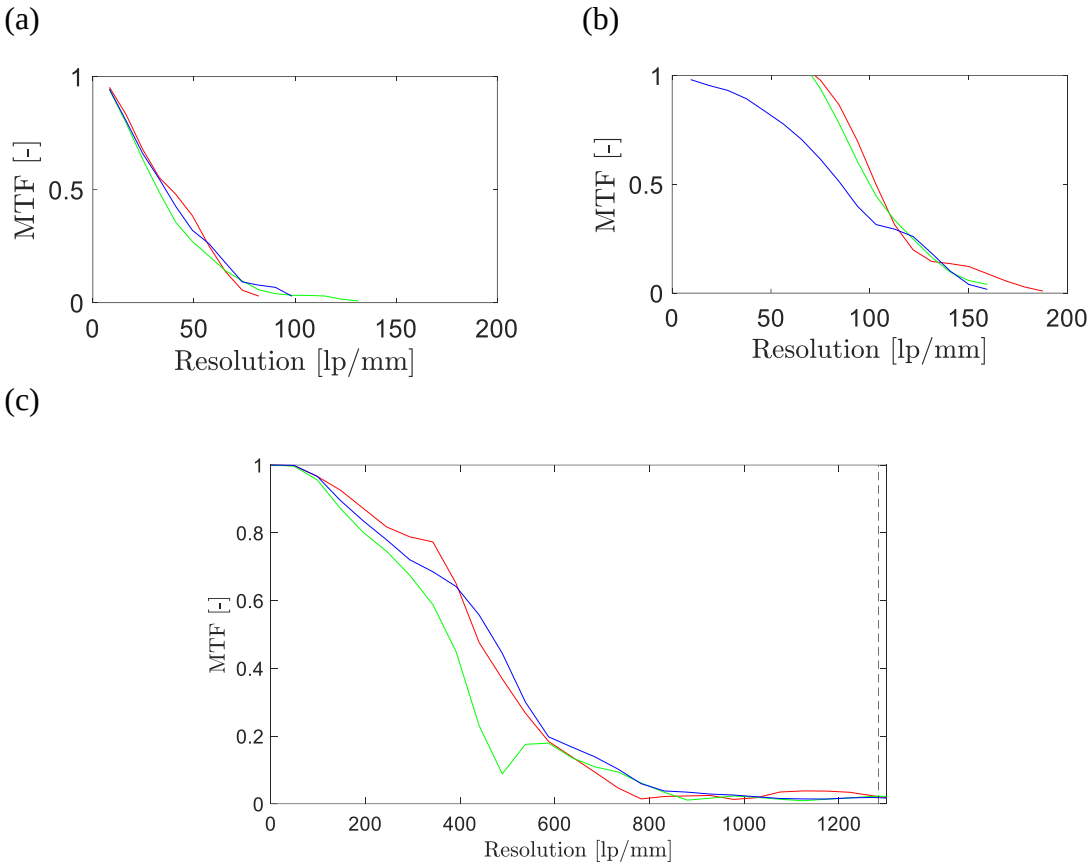

Figure 30: Measured MTF of the optical system with the (a) Questar QM-1, (b) 5x+200 mm lens, and (c) 10X+700 mm lens.

3.5.4 Depth of Field

The depth of field decreases with a high numerical aperture and decreases clarity in out of focus regions. The system used in phase 2 (10X + 700 mm lens) has a high NA of 0.28. Since the NA of the phase 2 system is higher than the phase 1 system, the depth of field was only quantified for the phase 2 system where it would be worse. To quantify the depth of field, the MTF as a function of object distance from the focal plane was measured in 10 μm increments. This is shown in Figure 31. The full resolving power is only achieved

for 10-20 μm of depth in each channel, making the imaging system difficult to focus. The system has at least 10 μm resolution for the spray width of 180 μm. Figure 31 also shows that despite using the Infinity K2S main lens, the phase 2 system exhibits negligible longitudinal chromatic aberration which is a problem when the K2S lens is used with the CF4 of CF1B objective [17].

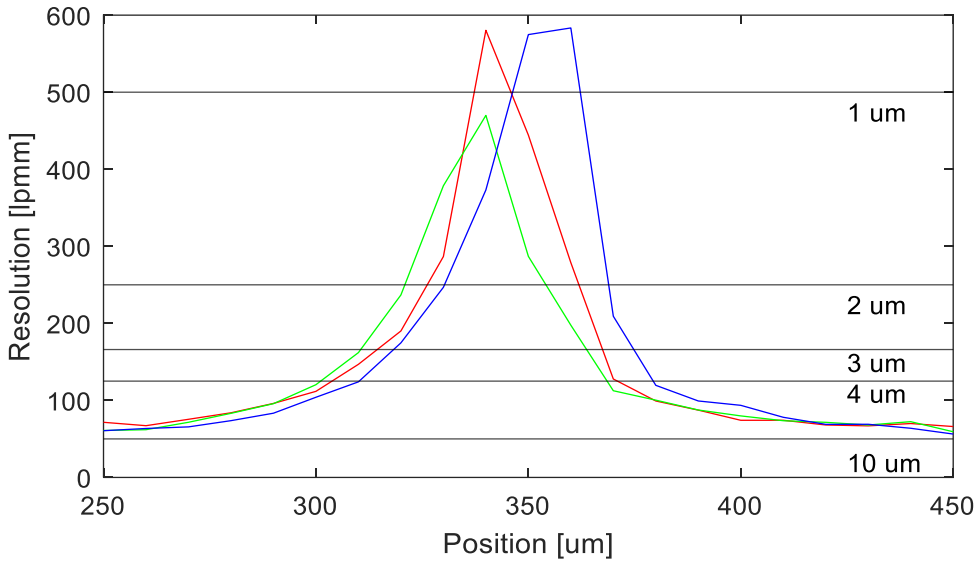

Figure 31: MTF for the phase 2 system as a function of focusing distance.

CHAPTER 4. RESULTS AND DISCUSSION

4.1 Experimental Spray Setup and Test Conditions

Engine-relevant atomization occurs at high pressures (> 10 bar), so an optically accessible vessel capable of high temperature and high pressures was used. The capabilities of this vessel are further detailed in [43]. The windows on this vessel also limit optical access.

The injector used in this study (ECN Spray D No. 133 [44]) has a 180 μm diameter nozzle and is supplied with n-dodecane fuel at pressures from 200 to 2000 bar. It is a scientific grade research injector used to standardize data collection. A schematic of the experimental setup including injector and fuel is shown in Figure 32. At a fuel pressure of 1500 bar, the fluid is travelling at Ma ~ 0.5, and undergoes as 12% expansion in density as it exits the nozzle.

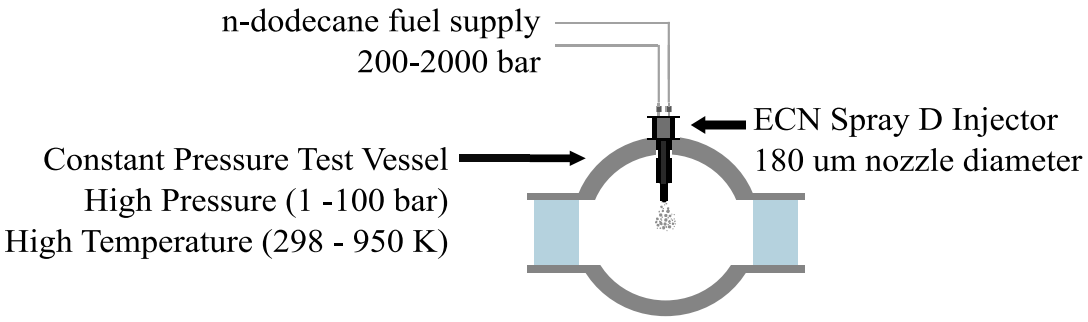

Figure 32: Experimental setup for studying atomization in engine relevant conditions.

Atomization in the Rayleigh, first wind, and second wind regime have all been well studied in the literature, but sprays in the atomization regime are not as well understood and are thus the subject of this work. All experiments in this work were performed with a

180 μm nozzle diameter and room temperature n-dodecane fuel, so the Ohnesorge number is constant at 0.021. The Reynolds numbers changed only with fuel pressure and air pressure and ranged from 31000 to 63000. All data was obtained with air at standard temperature (298 K) but varying pressures. The differences between phase 1 and phase 2 data sets, excluding lens design previously detailed, are detailed in Table 4.

Table 4: Operating condition difference between phase 1 and phase 2 data.

Data Set	Fuel Pressure [bar]	Air Pressure [bar]	Inter-frame delay [ns]
Phase 1	500,1000,1500	2,6,20	300
Phase 2	350,500,1000,1500	1	75

In Figure 33, the operating conditions for both sets of data are shown as black circles on the regime diagram from Reitz [45]. All test conditions are in the atomization regime.

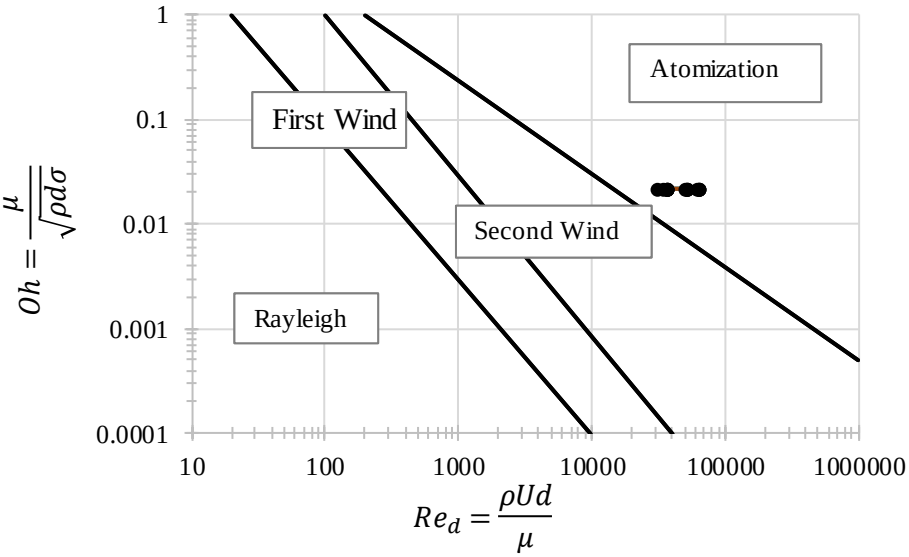

Figure 33: Test conditions in both phase 1 and phase 2 data set plotted as black circles. Regime diagram from Reitz [45]**.**

4.2 Sample Full Frame Images

The full frame resolution (6000 x 4000 pixels) and high repetition rate (10-20 Million fps) of this system can visualize spray phenomena previously impossible to see. Sample images from phase 1 and phase 2 are shown in Figure 34 and Figure 35, respectively. Figure 34 and Figure 35 show the immense field-of-view and resolving power that both systems are capable of. The change in magnification between the two setups changes the field of view, and the change in lens design changes the resolving power. For the two sprays shown in Figure 34 and Figure 35, the change in spray angle is attributed to the change in the ambient density. The blur from out of focus objects visible in Figure 35 is due to the narrower depth of field with the higher NA system, which is visible only with higher magnification.

Figure 34: Sample full frame (6000 px wide, cropped height) image from phase 1. Nozzle diameter of 180 μm, at 500 bar fuel pressure, 6 bar ambient pressure, 1ms ASOI. Nozzle diameter is 180 μm for scale.

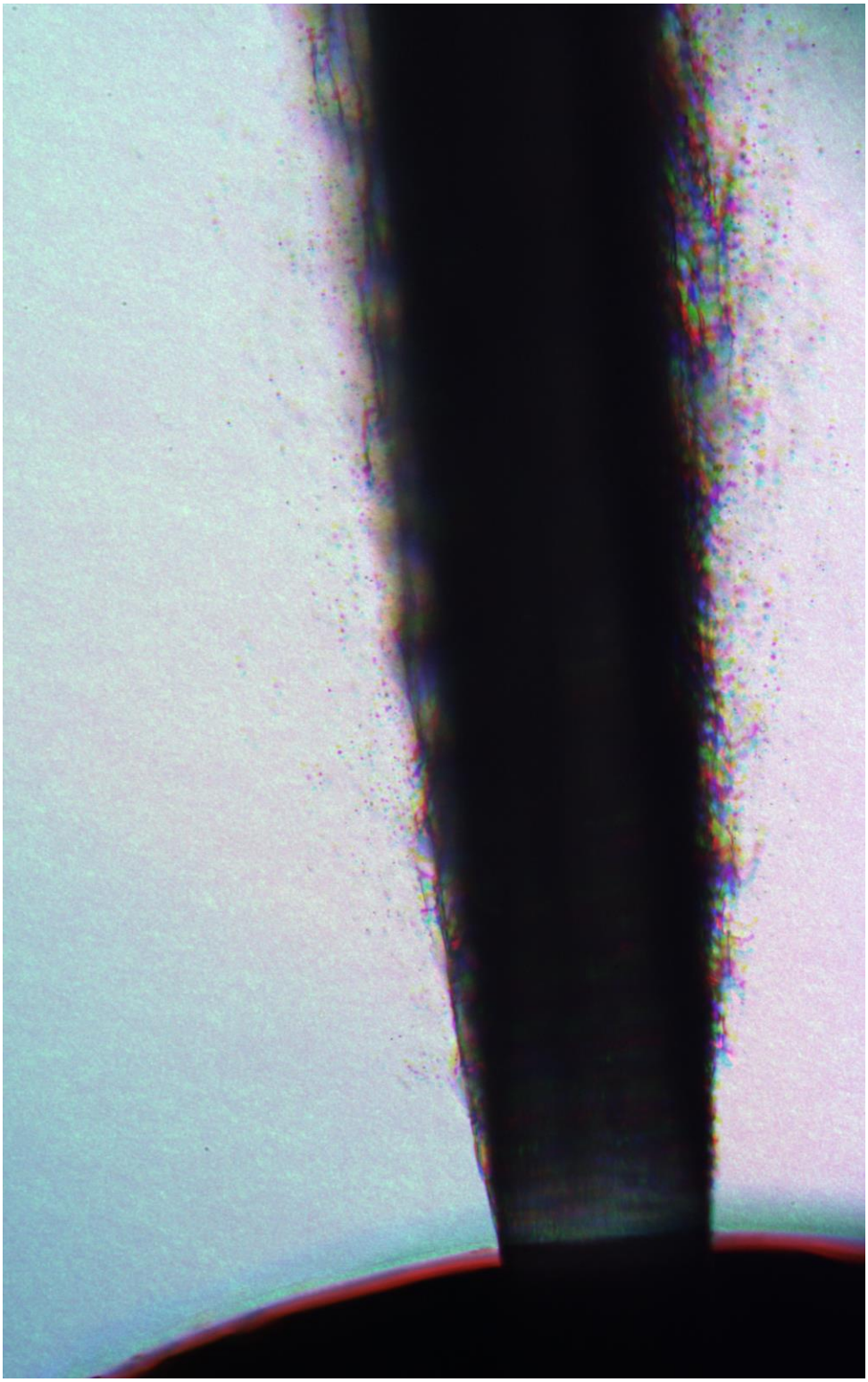

Figure 35: Sample full frame (6000 px wide, cropped height) image from phase 2. Nozzle diameter of 180 μm, 500 bar fuel pressure, 1 bar ambient pressure, 1 ms ASOI. Nozzle diameter is 180 μm for scale.

4.3 Initial spray formation

One phenomenon studied by many experimentalists is the shape of initial spray formation. The mushroom shaped structure of the initial low-velocity flow exiting the injector has been well studied and imaged at high magnifications and resolutions [18][46][47]. Images of this phenomena from the phase 1 data set are shown in Figure 36 and Figure 37. The same features noted by others are visible here such as the mushroom shape, leading ligament, and droplet formation underneath the mushroom.

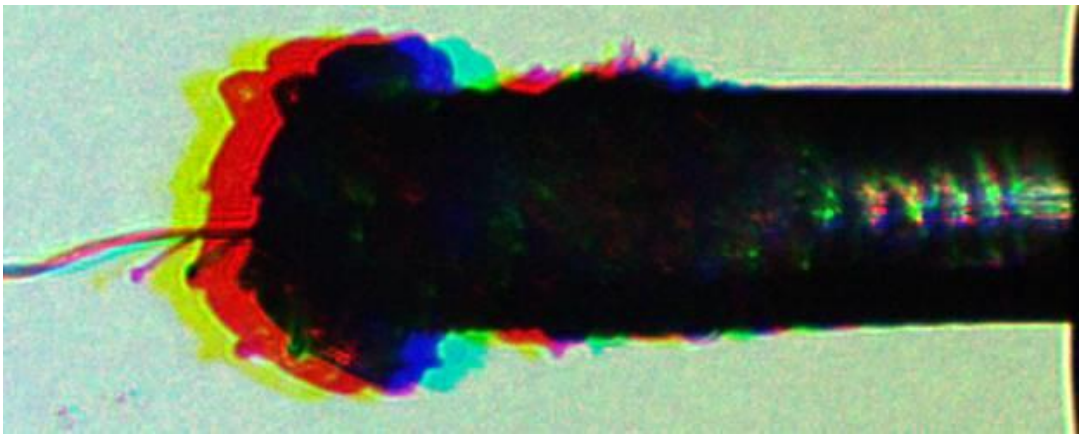

Figure 36: Initial spray formation from phase 1. Conditions are 500 bar fuel pressure and 6 bar ambient pressure. Images are taken 470μs ASOI, and nozzle diameter is 180 μm for scale.

Figure 36 and Figure 37 show a more chaotic structure compared to images by others, and this can be attributed to fuel property differences [18]. There is also evidence of a leading ligament development at the front of the spray undergoing a Plateau-Rayleigh instability to form droplets. Unfortunately, the resolving power of this system does not visualize droplet shape well so the phase 2 system was used for further imaging.

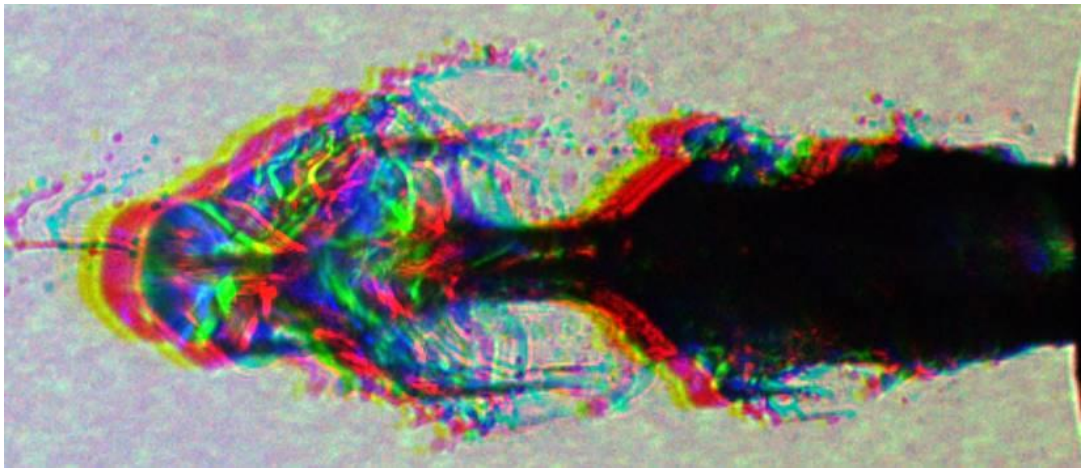

Figure 37: Initial spray formation from phase 1 images. Conditions are 500 bar fuel pressure and 2 bar ambient pressure. Images are taken 470μs ASOI, and nozzle diameter is 180 μm for scale.

One sample image from phase 2 is shown in Figure 38. In Figure 38, an illuminated area of the spray at nozzle exit is visible. Other works have noted the illuminated area at nozzle exit from backlit imaging configurations and hypothesized it is from both an intact liquid core and a lack of surface disturbances, as these would refract the light [48][49]. The application of Color-Coded Pulse-Burst Microscopy to quantify the intact liquid core is discussed further in section 4.4.

A total of 120 images of transient spray formation were taken in phase 2, with 30 images distributed between four fuel pressures. The images shown in Figure 38 - Figure 40 demonstrate the typical range of features seen during this initial injection period. An image obtained at 500 bar fuel pressure that shows the mushroom formation is shown in Figure 39. Another image taken at the same instance in time of another spray is shown in Figure 40. In Figure 39, the formation of the leading ligament is visualized but the leading ligament forms a second smaller mushroom shape.

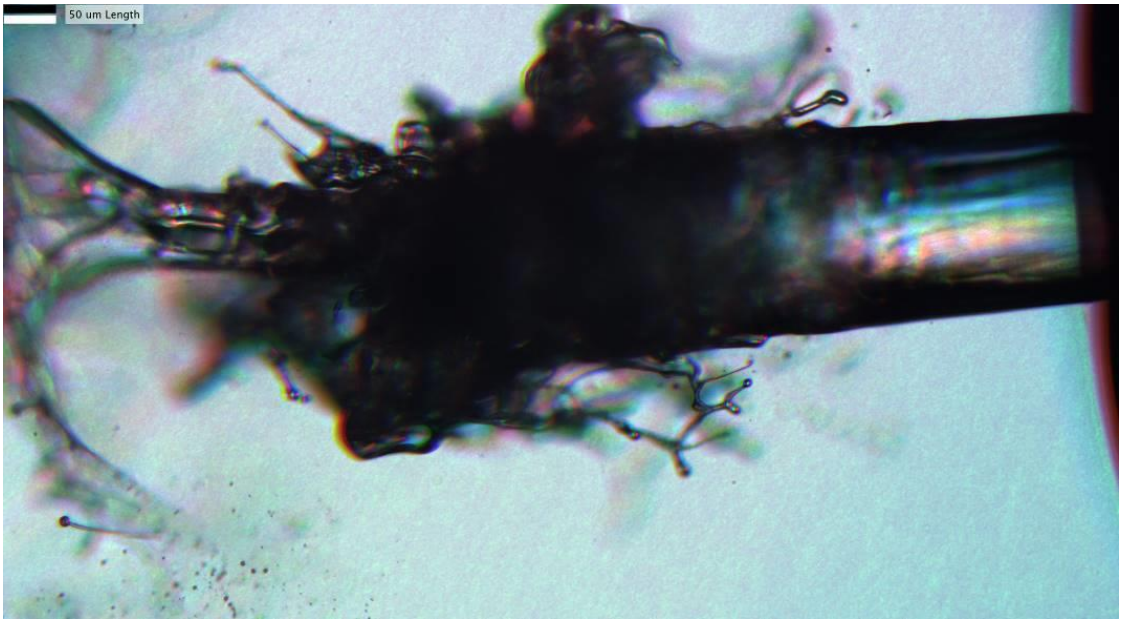

Figure 38: Initial spray formation from phase 2 images. Conditions are 350 bar fuel pressure injecting into STP air. Images are taken 245 μs ASOI, and the nozzle diameter is 180 μm.

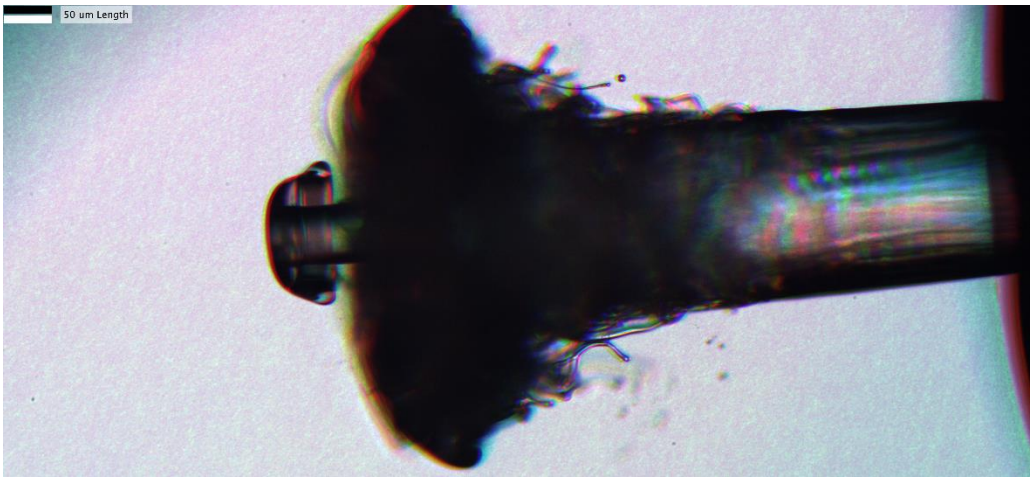

Figure 39: Initial spray formation from phase 2 images. Conditions are 500 bar fuel pressure injecting into STP air. Images are taken 210 μs ASOI and the nozzle diameter is 180 μm.

Figure 39 and Figure 40 also show ligament and droplet formation on the underside of the mushroom shapes. These droplet formations are the earliest atomization imaged in the sprays and appear to be cause by a Plateau-Rayleigh breakup from an elongated ligament.

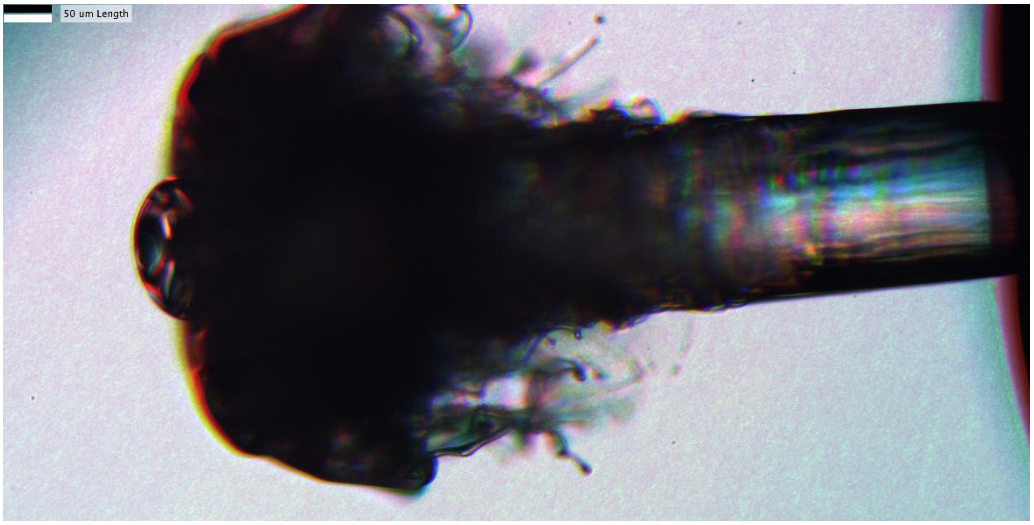

Figure 40: Initial spray formation from phase 2 images. Conditions are 500 bar fuel pressure injecting into STP air. Images are taken 210 µs ASOI, and the nozzle diameter is 180 µm.

4.4 Evidence for an Intact Core at Steady State Conditions

The existence of an intact liquid core at nozzle exit has been another area of research with atomizing sprays. Some have proposed that there is evidence of an intact liquid core at nozzle exit [50]. Yon et al. [49] noticed the illuminated core and hypothesized that visible streaks in the core came from cavitation. Pickett et al. [48] imaged "bright zones" near the nozzle exit, and hypothesized that this was due to a lack of a mixing layer, allowing the light to transmit through the liquid core uninterrupted like a lens. With the multi-piece high resolution lens, the intact liquid structure can now be well visualized. This was most easily seen at low fuel pressure transient events such as in Figure 41. Note the illuminated core and streak lines.

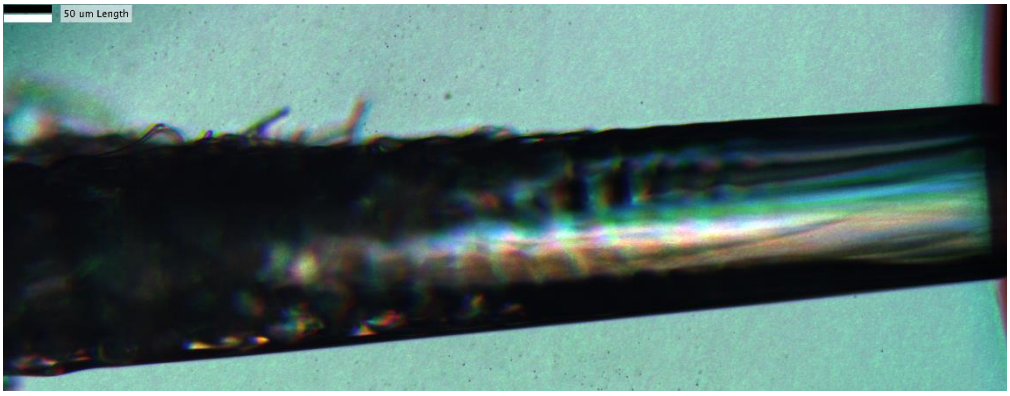

Figure 41: Initial spray formation from phase 2 images. Conditions are 350 bar fuel pressure injecting into STP air. Images are taken 250 µs ASOI, and the nozzle diameter is 180 µm.

Though more visible at lower fuel pressure transient events, the structure was also noticed at high pressure steady state events. An image of the intact core at 350 bar fuel pressure in a steady state event is shown in Figure 42. Figure 42 again shows the presence of streaks along the flow direction at the nozzle exit and shows the illuminated area at the nozzle exit indicating an unbroken liquid core.

At higher fuel pressures the light passing through the intact core diminishes. This is shown in Figure 43. One hypothesis that aligns with Pickett's theory is that the higher fuel pressures causes atomization to begin closer to the nozzle exit so light does not pass through the core. To better visualize the intact core and initial atomization of the spray, a novel illumination technique is needed. Early experimentation with the inclusion of a near-field diffuser has revealed structures of these high-pressure microscopic sprays previous hidden. This is discussed in the following section.

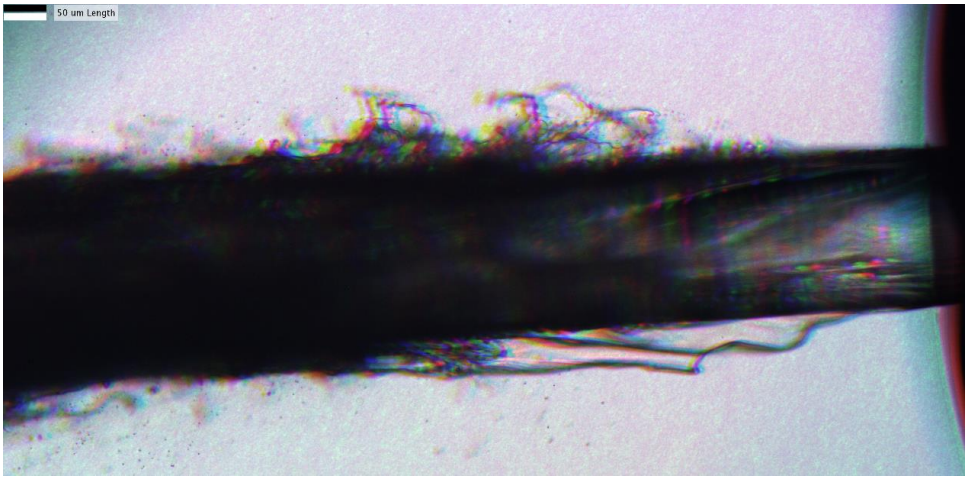

Figure 42: Spray formation from phase 2 images. Conditions are 300 bar fuel pressure injecting into STP air. Images are taken 1ms ASOI, and the nozzle diameter is 180 µm.

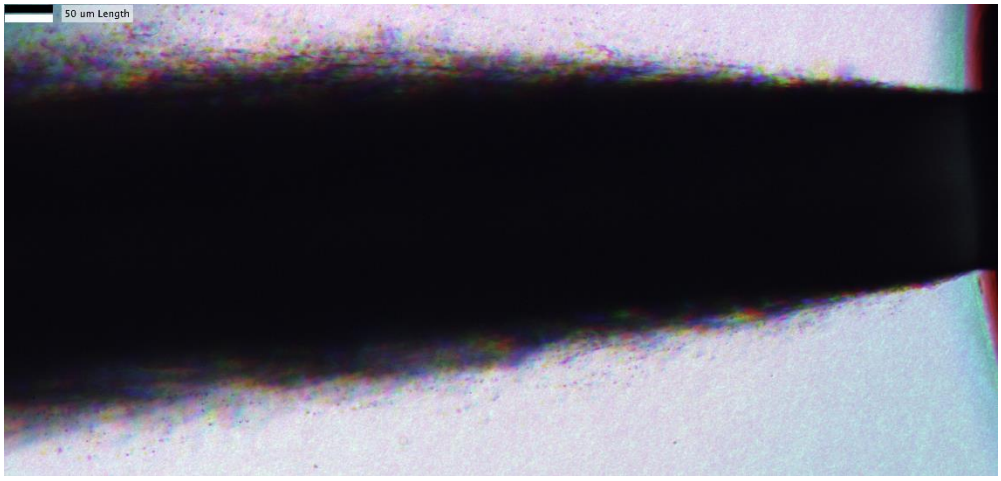

Figure 43: Spray formation from phase 2 images. Conditions are 1500 bar fuel pressure injecting into STP air. Images are taken 1ms ASOI, and the nozzle diameter is 180 µm.

4.5 Visualization of Periodic Surface Instabilities

The prevailing atomization theory, the K-H breakup theory by Reitz [45], suggest that primary atomization occurs from surface Kelvin-Helmholtz instabilities that form droplets with diameters on the order of the fastest growing wavelength (Figure 4). This theory suggests micron or sub-micron scale droplets exist in engine relevant conditions,

and it has been difficult to validate due to optical thickness of the sprays and the resolving power of high-speed imaging systems. However, at certain conditions the intact liquid core discussed in the previous section exhibited periodic surface features. Previous work by Hoyt and Taylor [51] showed these same structures with visible connections to instabilities on the spray periphery.

An example of these instabilities is shown in Figure 44. Here, the red, green, and blue banding show the structure moving in time. In Figure 44 there is a small blurry surface disturbance at the top spray edge. The size and spacing of this disturbance on the edge correlate with the disturbances on the front of the spray, indicating they may be linked.

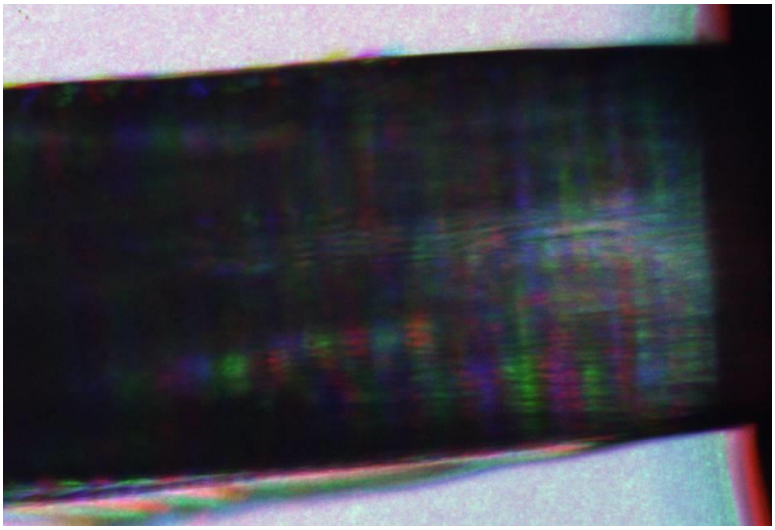

Figure 44: Surface waves at nozzle exit. Image taken at steady state conditions with 300 bar fuel pressure. Images are taken with the phase 2 system 1ms ASOI, injecting into air at STP.

The wavelengths shown in these images are on the order of 10 μm rather than the order of 1 μm proposed by Reitz [45]. While the image shown in Figure 44 was taken in phase 2 and is highly resolvable, earlier images from phase 1 were used for analysis as they were taken at varying air pressures. A sample image from phase 1 is shown in Figure 45.

Here the instabilities are still resolved despite the lower system resolving power of 3 μm because the wavelengths are on the order of 10-20 μm.

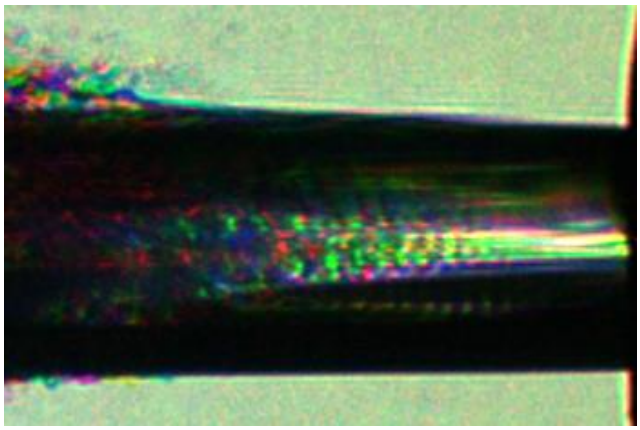

Figure 45: Surface waves at nozzle exit taken with the phase 1 setup. Image taken at steady state conditions with 500 bar fuel pressure injecting into 6 bar ambient pressure.

The surface wavelengths for each image were manually measure at all steady state conditions for images from phase 1. The average visible surface wavelength for each condition was then compared to theoretical quantities. The first quantity to compare the measured wavelengths to was the prediction by the Kelvin-Helmholtz model [52]. This comparison is shown in Figure 46.

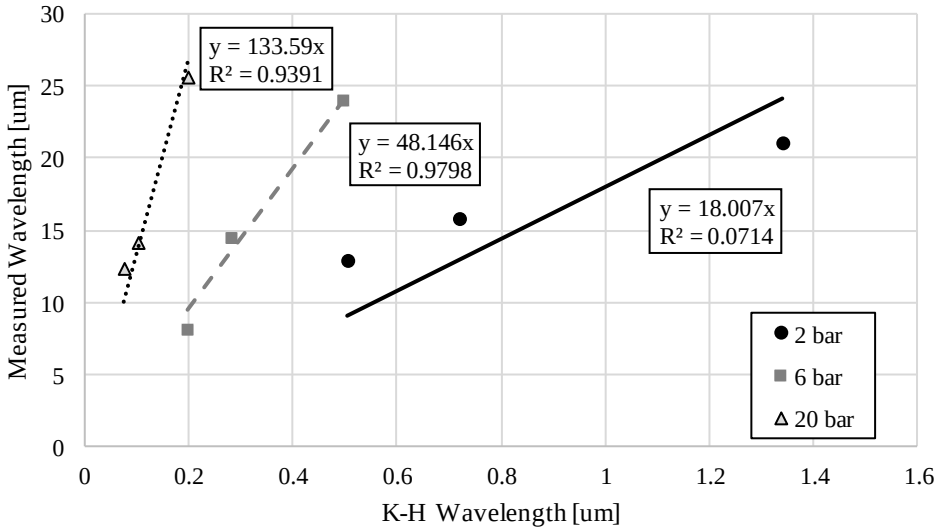

Figure 46: K-H predicted wavelength relative to measured surface wavelength from phase 1 images of steady state injections.

In Figure 46, a linear relationship between the predicted fastest-growing wavelength and the measured wavelength is evident at a given ambient pressure. The correlation strength at 2 bar ambient pressure is the weakest, which is intuitive as lower ambient pressures would reduce aerodynamic K-H breakup. The slope of the relationship also increases with ambient pressure, signifying there is a way to collapse these to one correlation.

The measured wavelengths (O ~ 10-20 μm) are an order of magnitude larger than those predicted by the K-H model (O ~ 1 μm). One hypothesis for this is that the instabilities are not K-H surface instabilities but rather a different fluid instability. This is supported by the shape of structures on the spray periphery shown in Figure 42, which do not resemble K-H instabilities but instead appear to be long, stochastic ligaments with diameters, not lengths, on the order of $1\mu m$ as predicted by the K-H model. Cavitation could be theorized to be the source of these wavelengths, as streak lines on the surface of

the jet could be indicative of internal cavitation [49]. Another potential source would be periodic expansion waves caused by fluid compressibility, but these would be travelling down the jet at approximately twice the speed of the jet, and there is little evidence to suggest this is occurring. Further research on the source of these disturbances is necessary to quantify the sources.

The three correlations in Figure 46 vary with ambient pressure, and an attempt was made to collapse them onto a single relationship from known turbulence quantities. It was determined that the ratio of the Reynolds number to the Weber number collapsed the three correlations. This is shown in Figure 47, and a linear trend line was fitted to show the strength of the correlation. This non-dimensional quantity is only a function of the fluid properties (unchanged in the experiments) and velocity, shown in Eq. (13). To validate this model different fuels would need to be tested.

$$\frac{Re}{We} = \frac{\sigma}{\mu v} \tag{13}$$

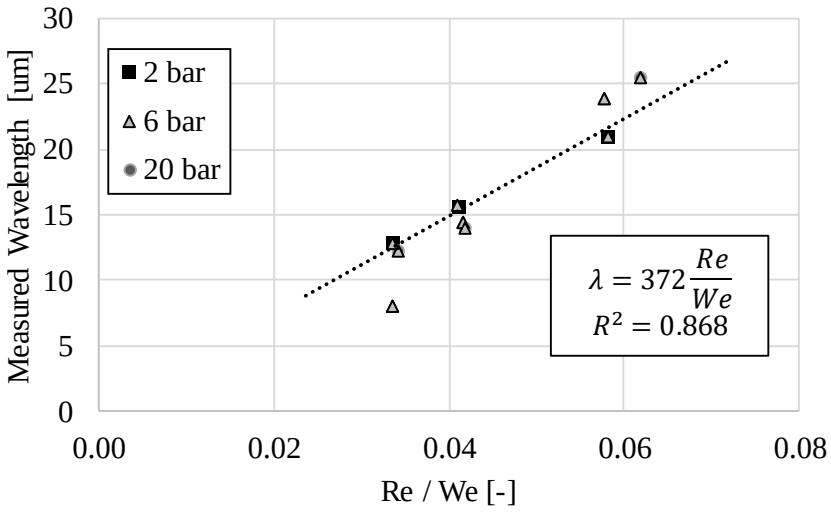

Figure 47: Measured surface wavelength compared to the Reynolds number over the liquid weber number

The surface instabilities vary in predicted wavelength from the prediction by the K-H aerodynamic model, and the visualization shows longer ligaments rather than a traditional K-H shape. This indicates the breakup may not be aerodynamically driven but could be driven by turbulence, cavitation, or internal resonance in the injector. Internal pressure variations have been measured previously to be on the order of 1-10 kHz [53], while the waves measured in this study have oscillation on the order of 10-100 MHz, indicating they are not driven by pressure variations in the nozzle.

To better visualize the surface instabilities, an imaging technique was used where a diffuser was placed directly adjacent to and in proximity behind the nozzle, called a "near field diffuser". Preliminary images using the near field diffuser illuminate the intact liquid core brighter than images without the diffuser. A diffuser increases the ratio of diffuse light to non-refracted light, thus reducing the effect of beam steering along edges of features. This in turn illuminates the spray core showing surface instabilities further downstream than previous images. An image taken with a near field diffuser is shown in Figure 48. Figure 48 is not well focused, as it was taken with a prototype lens setup that was not well aligned. In future work, this system could be improved, and more detailed images of the liquid core and surface instabilities could be obtained.

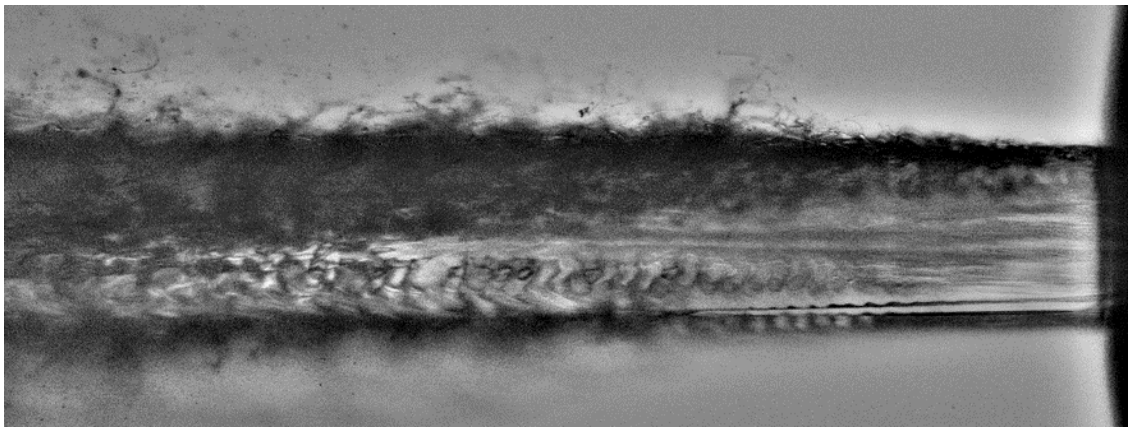

Figure 48: Monochromatic image of a Spray D injection at 400 bar fuel pressure injecting into ambient air, 1ms into a 2ms injection event. Some of the features on the top of the spray near nozzle exit are in focus as are some features downstream in the center of the spray, but the lower edge of the spray is out of focus.

In Figure 48, a few features of the spray are noticed. These are the intact core at nozzle exit and the sinusoidal surface instabilities on the front surface of the spray. The intact core protrudes further downstream than previous images show (Figure 42). Periodic disturbances, seen both on the top and on the front of the spray, initiate at a point and propagate along the cylindrical stream axially and angularly. The disturbance on the front surface has a corresponding wavelength on the order of 10 μm.

The disturbance initiating at the top of the spray is likely from nozzle defects in the ECN spray D No. 133 injector used in this experiment. Work by Magnotti et al. imaged the injector used in this experiment with x-ray tomography and showed a prominent ridge in the nozzle which could cause this disturbance [54]. To validate this, the injector was rotated and imaged at 3 orientations, and this disturbance moved with the nozzle indicating it is geometrically driven.

4.6 Droplet and Ligament Breakup in Primary Atomization

Primary atomization is difficult to study because it is difficult to resolve the microscopic fluid objects at high framing rates. Work by Wu and Faeth resolved primary atomization, but observed nozzle diameters and atomization features on the mm scale [11], [55]. While work has been done to observe primary atomization in real engine conditions [18], [19], these experiments have not had the performance required in Table 3, limiting the applicability of the results. In this work, over 250 images were obtained during phase 2 with two spray timings (steady state and transient injection periods) and 4 fuel pressures (300,500,1000, and 1500 bar). This allows a qualitative analysis on the effects of varying conditions on primary atomization and a discussion of the phenomena visualized.

A set of sample images from the low fuel pressure (300 bar) case at steady state is shown in Figure 49. Here, the images have a 2 μm square at the top left and are taken 75 ns apart. Anecdotally shown is that there were no discernable images of a K-H instability on the spray periphery within six nozzle diameters downstream of the injector orifice. Most images show drop formation as secondary breakup from a long ligament. This is exemplified in Figure 49 (c) and (e). This breakup has been observed by others, and was described as Cigar-shaped breakup by Hinze in 1955 [56].

The scale of atomization is also another point of interest. In Figure 49 (a), (d), and (e), most droplets are on the scale of 2-10 microns, while the ligaments that form them are similar diameter but on the order of 10-50 μm long.

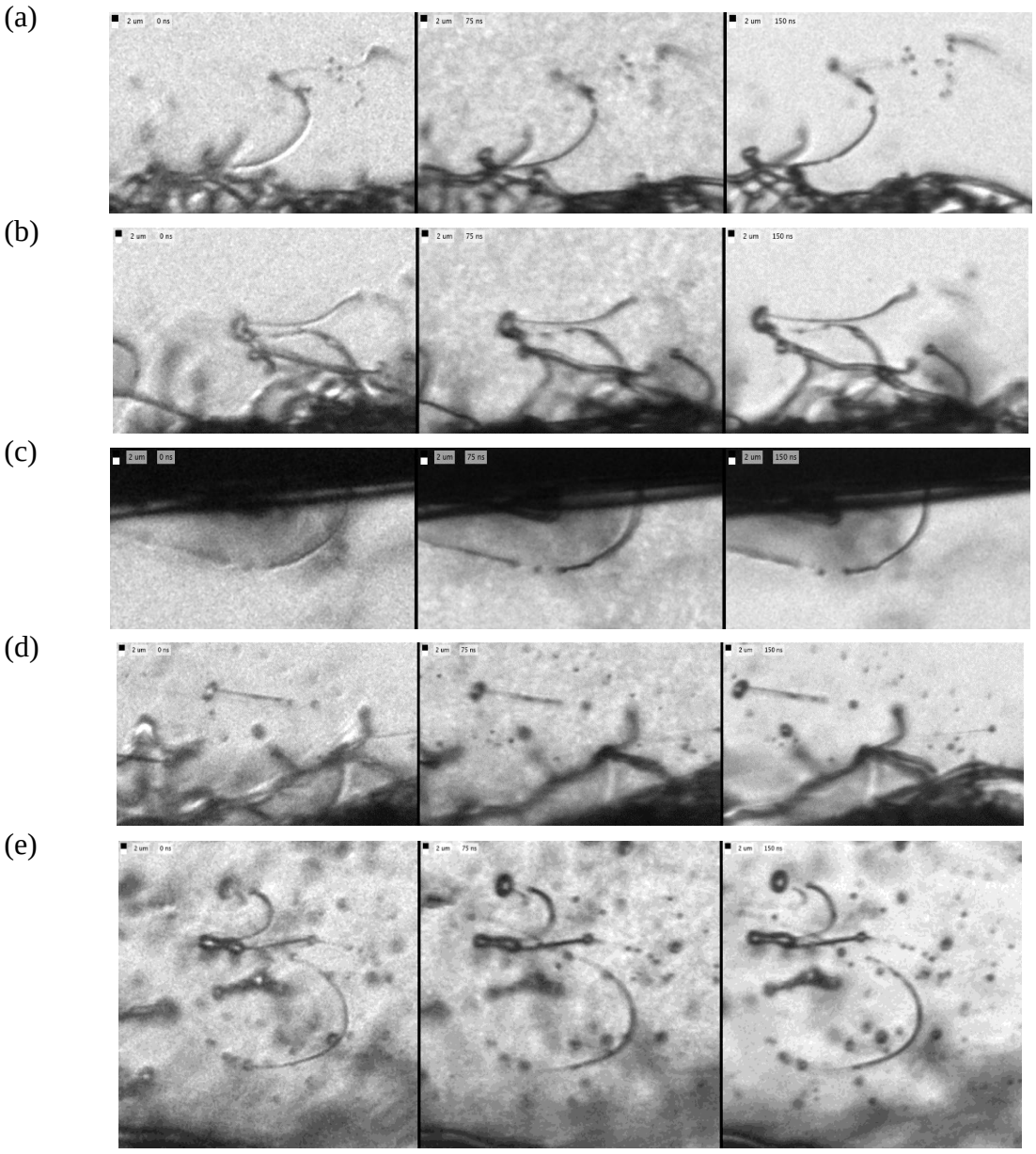

Figure 49: Primary atomization on the periphery of the spray at 300 bar fuel pressure, steady state conditions. The adjactent black and white squres visible at the top left of each image are 2 μm x 2 μm wide, and the images are taken at 0, 75, and 150 ns (left to right) after the first exposure

Figure 49 (a) shows a ligament being ejected from the spray, and they break into collinear ligaments and droplets via a Plateau-Rayleigh instability. A similar phenomenon is shown in Figure 49 (b). This was a common observation through the data set. Figure 49 (c) shows the Plateau-Rayleigh instability on another long ligament. A typical droplet field

on the spray periphery is shown in Figure 49 (d) and (e). The out of focus features are prevalent behind the in-focus objects.

Figure 50 shows more images of primary atomization but at fuel pressures of 500 bar. Figure 50 (a) shows a typical droplet/ligament field around the spray periphery. Note the ligament being ejected from the surface in the middle of the images. Figure 50 (b) shows a droplet formation from a long ligament. The ligament (formed by an unknown phenomena) is undergoing a Plateau-Rayleigh instability, and droplet formation at the end of the ligament is seen in the three images.

Figure 50 (c) shows a ligament with diameters on the order of 1-2 μm breaking off perpendicular to the jet stream, with the end pinching off to forming a shorter ligament. Droplets from secondary breakup are also seen around the ligament. Figure 50 (d) shows the formation of a droplet, coming from a Plateau-Rayleigh instability on a ligament breaking away from the spray. The droplet diameter has decreased compared to Figure 49, aligning with prevailing atomization theories.

(a)

(b)

(c)

(d)

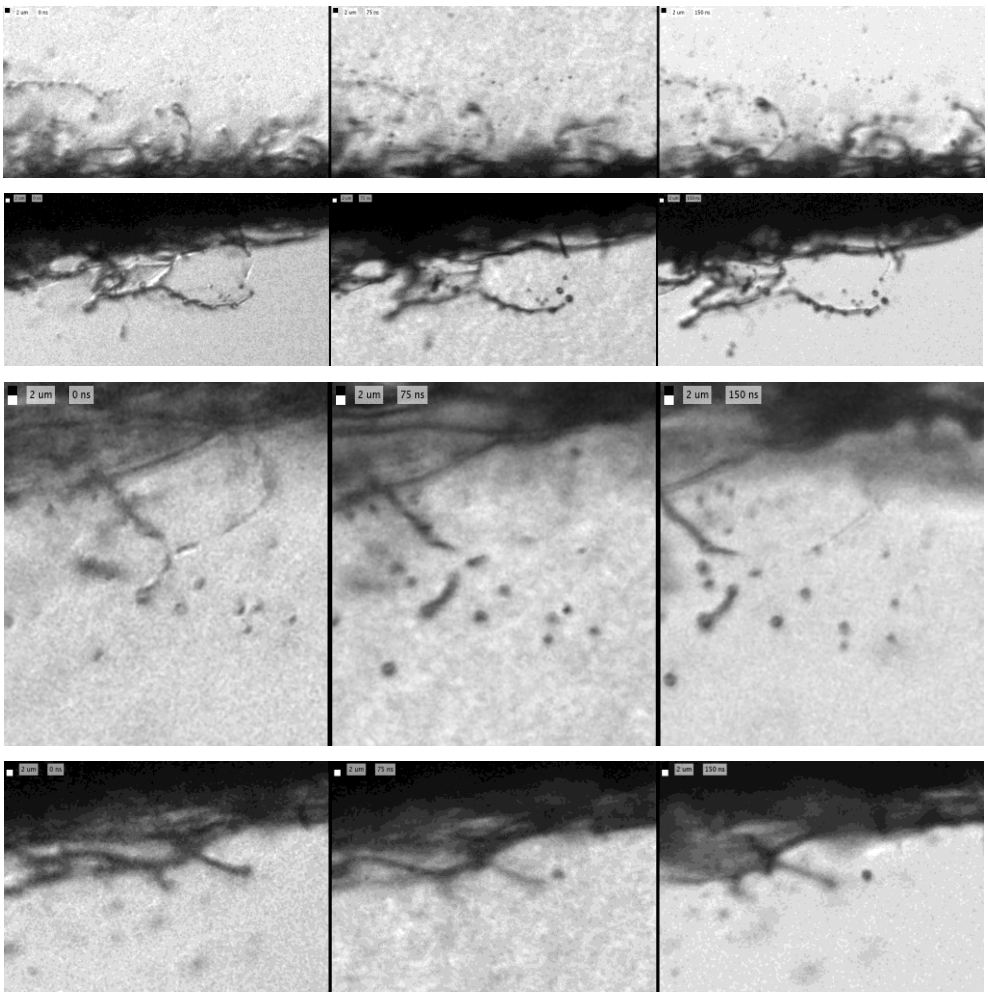

Figure 50: Primary atomization on the periphery of the spray at 500 bar fuel pressure, steady state conditions. The adjactent black and white squres visible at the top left of each image are 2 μm x 2 μm wide, and the images are taken at 0, 75, and 150 ns (left to right) after the first exposure

Figure 51 shows primary atomization at 1000 bar fuel pressure. In Figure 51 (a), a long ligament undergoing Plateau-Rayleigh instability forms droplets during the three frames. Figure 51 (b) shows multiple ligaments being ejected from the spray surface, and these appear similar to the ligaments imaged by Wu and Faeth [11].

Figure 51 (c) and (d) show an interesting phenomenon noticed during experimentation occurring at nozzle exit. On the bottom edge of the nozzle at higher fuel

pressures, a long ligament tends to form at a slight angle from the spray. This could be due to a microscopic manufacturing defect in the nozzle. These long ligaments are initiated at a similar location in every injection and result in a near-nozzle droplet generation on the μm scale.

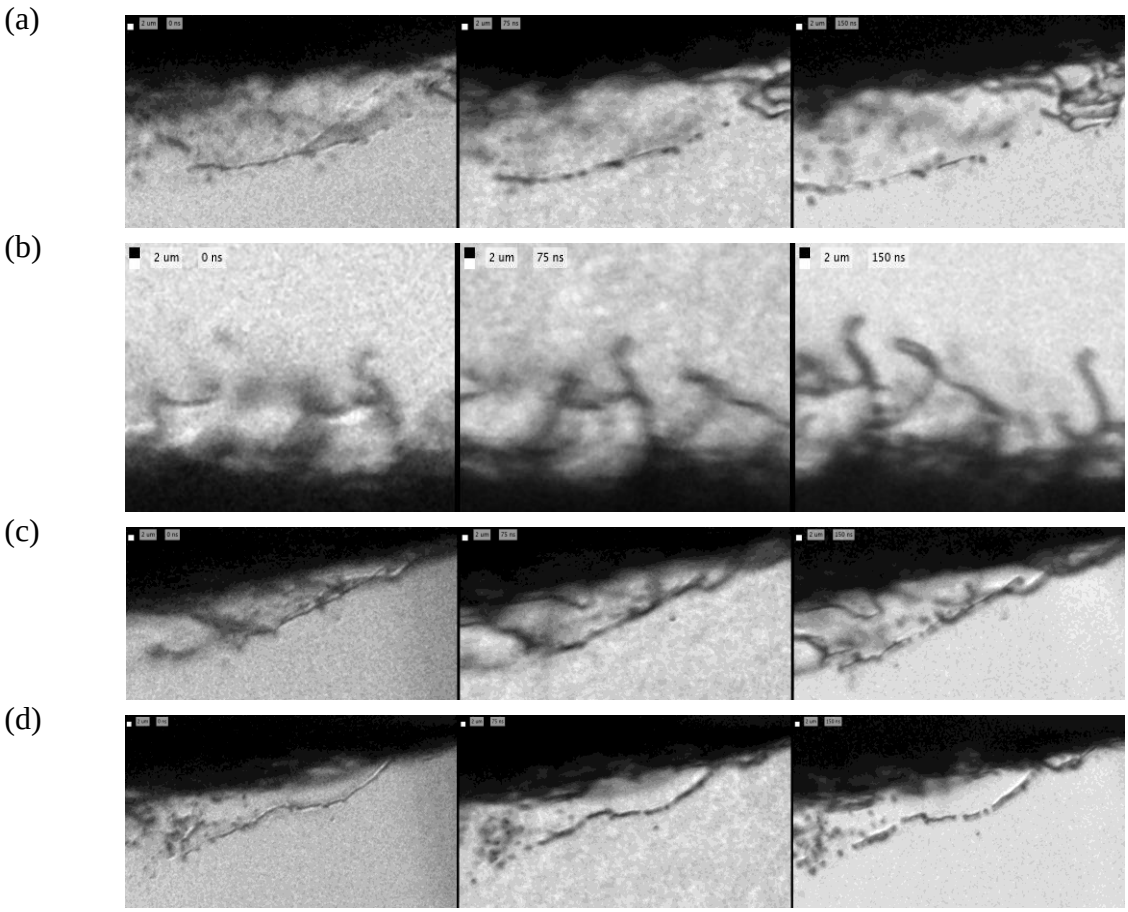

Figure 51: Primary atomization on the periphery of a spray at 1000 bar fuel pressure, steady state conditions, injecting into air at STP. The adjactent black and white squres visible at the top left of each image are 2 μm x 2 μm wide, and the images are taken at 0, 75, and 150 ns (left to right) after the first exposure

As fuel pressure increases above 1000 bar, the scale of atomization decreases and structures in the image are difficult to resolve. Of the 30 full frame images taken at steady state with 1500 bar fuel pressure, the three clearest instances of drop formation are shown in Figure 52. Most spray features were smaller than the resolving power of the system. In

Figure 52(a) and (b), the near nozzle droplet generation is visualized once again, but droplets and ligament diameters are smaller than the resolving power of the system, making them appear as airy disks. Figure 52 (c) shows a series of ligaments being ejected from the spray surface, but these are also poorly resolved by the imaging system. This could indicate the presence of sub-micron droplets as theorized by Reitz et al. [52].

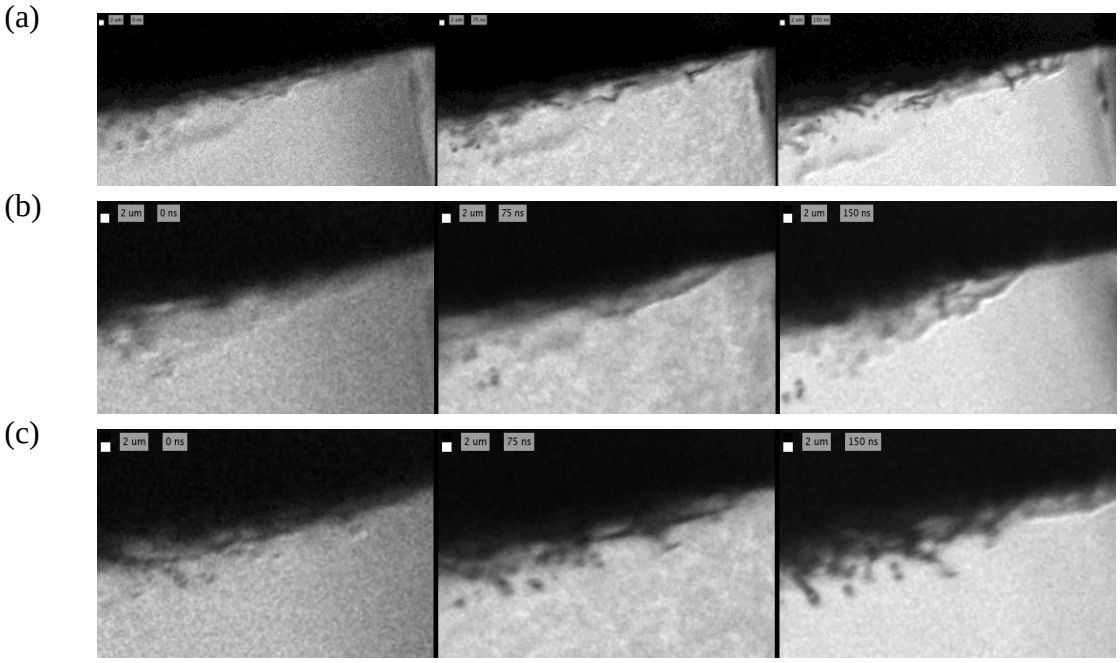

Figure 52: Primary atomization on the periphery of the spray at 1500 bar fuel pressure, steady state conditions.

CHAPTER 5. FUTURE WORK

5.1 Improved Test Conditions

One drawback of the image set is that phase 1 is that they were not taken at engine relevant temperature, and phase 2 images were taken at neither engine relevant temperature more pressure. To gather data on engine relevant conditions, the spray must be imaged at elevated temperature and pressure. While the remote objective concept has been used at higher pressure, high temperature presents a new set of challenges. One of these is the usage of the microscope objective outside of their designed case. It is unlikely that image quality from the system will remain on the micron scale at the elevated temperatures due to component expansion and the effect of beam steering. One way to overcome this would be to design a custom objective lens. Two opportunities for this are realized.

5.2 Optical System Changes

Having reverse engineered the Infinity K2S microscopic lens, a few recommendations for future lens design and selection can be made. The remote objective concept may not work at elevated temperature. Two potential solutions exist for this. First, a custom objective lens could be designed that could withstand high working temperature and maintain focus. This could be done with a high temperature achromatic lens, but questions remain as to the availability of these lenses. To replicate the 10X objective, a focal length of approximately 35 mm would be needed.

Another solution is the construction of a custom long working distance microscopic lens. The performance of a custom lens is from the quality of the lenses, the focal length

ratio of the main lens to the objective lens, and the numerical aperture of the objective lens. A lens could be constructed that is optimized for the optical access in the vessel. To optimize the numerical aperture of the lens, and effective focal length for the objective would need to be approximately 300-350mm, with a diameter as wide as the vessel window (approx. 150 mm). This could be achieved with telescope objective lenses. Scientific grade lenses that meet these requirements exist for a price, and a cost-effective solution exists at websites such as Surplus Shed. To use the large numerical aperture of the objective lens, it is theorized that a large diameter main lens is necessary. A Nikon 400 mm F/2.8 lens would provide nearly full field of view of the objective lens and window and could be coupled with tele-converters to increase the magnification as needed. With a 400 mm lens, a 300 mm objective, and two 2X teleconverters, the Abbe and Nyquist limit would both be approximately 1.4 μm.

5.3 Incremental System Improvements

While the Color-Coded Pulse-Burst Microscopy system detailed here is high performance and well optimized, there exist incremental improvements that could be made to the imaging system. Two of these improvements are related to the imaging camera system and the illumination power and pulse width. A Bayer filter array camera was chosen early on for this project and functioned well at high magnifications. However, recent development with the Foveon imaging sensor has made it practical for use in Color-Coded Pulse-Burst Microscopy. Foveon sensors utilize a three-layer sensor, with red, green, and blue pixels stacked on top of one another as opposed to side by side. This reduces defringing aberrations, a problem on the pixel scale in Color-Coded Pulse-Burst Microscopy [57][58]. For higher magnifications above the Abbe limit (such as

0.2 $\mu m/px$), the defringing effect is less pronounced and the advantage of the Foveon sensor is negated. A Foveon sensor would also introduce the problem of lens compatibility as they often use a proprietary and uncommon Sigma lens mount.

Another improvement to the Color-Coded Pulse-Burst Microscopy system would be the usage of a picosecond laser. While the nanosecond ND:YAG Laser provided sufficient power and was able to freeze structures on the periphery of the spray, there was still motion blur in the smaller and faster features at higher fuel pressures and higher air pressures. Other work in the literature has shown the advantage of a picosecond laser for spray illumination as opposed to nanosecond illumination [30]. If this were to be implemented with Color-Coded Pulse-Burst Microscopy, the system would resolve clearer images by reducing motion blur.

5.4 Data Processing

Further work could also be accomplished on post-processing the images obtained in phase 2. One challenges to this is droplet sizing and tracking. A machine learning program would be a solution to this and could be used to process hundreds and thousands of images. However, machine learning takes considerable time and effort to train and requires a very large data set. A traditional edge detection approach is more feasible.

Edge detection and sizing calculations benefit from magnifying the drops to appear as airy disk. Techniques such as wavelet analysis could be used to interpolate an edge location, where edge information is obtained from neighbouring pixels. This increases information available for an edge detection algorithm and has been shown to increase the reliability of droplet edge detections [59]. Once droplet size and position are determined, a

tracking program can be coded to analyse droplet velocities and acceleration. A prototype for this code was constructed and used the lower resolution photos from the phase 1 data set, but it showed velocities significantly lower than the Bernoulli velocity which questioned the reliability of the program.

The images from phase 2 can size droplets larger than 1.2 μm, and could thereby determine the Sauter Mean Diameter on the periphery of the spray. An attempt at quantifying this was performed with the phase 1 data set, but due to relatively low image resolution, the results were deemed irrelevant. Adapting this code to the images from phase 2 proved difficult as new challenges were encountered with high magnification droplet identification.

5.5 Plenoptic Imaging as a Compliment to Color-Coded Pulse-Burst Microscopy

All previous improvements optimize 2-dimensional Color-Coded Pulse-Burst Microscopy. One beneficial and novel way to leverage Color-Coded Pulse-Burst Microscopy is with a Plenoptic camera, which requires a high-resolution image sensor. Plenoptic cameras use an array of microlenses to image an event from multiple perspectives. This opens up new possibilities with post processing [60], [61]. Effects like changing perspective, refocusing after imaging, increased depth of field, and measuring depth are possible with Plenoptic cameras. Although microscopes using Plenoptic cameras have been created [62], they have do not resolve the micron scale and have only been used on single shot, non-moving objects. More details on a Plenoptic Microscopy setup for studying primary atomization with preliminary images can be found in Appendix A.

CHAPTER 6. CONCLUSIONS

6.1 Imaging System Design and Performance

In this work, a high-performance Color-Coded Pulse-Burst Microscopy imaging system is designed and implemented to study primary atomization. A custom multipiece imaging lens is designed and used to resolve objects on the scale of 1.2 μm with an image resolution of 0.2 $\mu m/px$. This is coupled to a consumer grade Nikon D5300 DSLR color camera, and with a high-speed, high-power illumination system, captures three 24 Megapixel images fully exposed with 5ns exposure times. A Color-Coded Pulse-Burst Microscopy system was then designed around the color camera using tuned Laser Induced Fluorescent dyes so that a 3 frame, 20 million fps video can be taken with a single shot of the system. Further work incorporating a near field diffuser and analysing its effects on microscopic spray imaging was also accomplished.

A comparison of the system used in this work to systems used in other state of the art high speed microscopy applications is given in Table 5. The high-performance Color-Coded Pulse-Burst Microscopy system has the largest image size, shortest exposure, highest resolution, and can be adjusted to match or exceed the highest framerate. Color-Coded Pulse-Burst Microscopy has the best performance of any imaging system and allows the study of primary atomization in ways not previously possible.

Table 5: Comparison of microscopy capabilities of high-performance Color-Coded Pulse-Burst Microscopy to other imaging technology used in the literature

	Exposure	Image Size	Frame Rate	Resolution
Zaheer [16]	20 ns	128 x 48 px	480 kfps	9.8 μm
Kim [17]	33 ns	6000 x 4000 px	1 Mfps	2 – 4 μm
Crua et al. [18]	20 ns	1280 x 960 px	200 Mfps	2.3 μm
Kirsch et al. [19]	10 ns	1024 x 1280 px	1 Mfps	2 μm
Phase 1	5 ns	6000 x 4000 px	3 Mfps	3.8 μm
Phase 2	5 ns	6000 x 4000 px	13 Mfps	1.2 μm

6.2 Critiques of Current Models of Primary Atomization

The images shown in Figure 49 through Figure 52 show multiple noteworthy features. In most cases, primary atomization forms long ligaments rather than spherical droplets, and these ligaments only turn into droplets upon secondary breakup, which was commonly observed as Plateau-Rayleigh, sheet and bag breakup. These longer ligaments show that the assumption of spherical droplets in primary atomization needs to be evaluated. The intact liquid core of the spray was validated at fuel pressures of 300 bar, which is in the atomization regime. Visualization of the intact core at 400 bar was then accomplished using a near-field diffuser, and this sheds light on the development of periodic surface instabilities on the spray. Finally, images of potential sub-micron droplets potentially validate parts of the K-H model.

APPENDIX A. RUDIMENTARY HIGH SPEED PLENOPTIC MICROSCOPY

A rudimentary Plenoptic imaging setup was created and used for imaging the Spray D injector and a USAF test target. This setup is shown in Figure A.1, where a Lytro Illum is the Plenoptic camera, and a relay lens (50mm f/2), is connected to the Infinity K2S lens with the Infinity CF4 5X objective. The system shown in Figure A.1 was improved upon in multiple ways. A 135mm f/2 relay lens replaced the 50mm f/2 lens to lower the magnification to fit the spray diameter in the image and to reduce the vignette on the images. To correct for chromatic aberration, the 10X long working distance objective replaced the Infinity CF4 5X objective. This system was then used with the Color-Coded Pulse-Burst Microscopy system to obtain the world's first high resolution, high speed Plenoptic images.

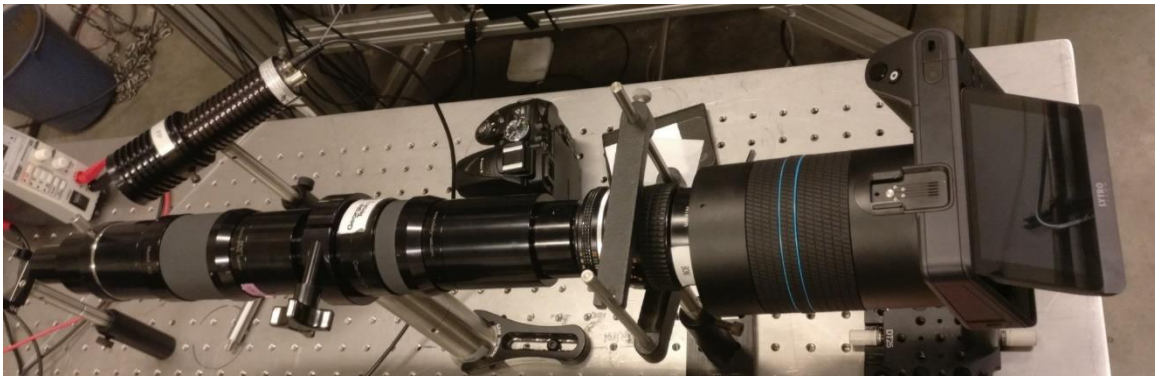

Figure A.1 Early Plenoptic imaging setup using a Lytro Illum, 50mm f/2 relay lens, and infinity K-2S main lens with the 5X CF4 objective.

The Lytro Illum outputs files that are a proprietary image format, but these have been reverse engineered and can be used with the Light Field Toolbox in MATLAB [63]. This toolbox turns the Light Field images into a 2-D array of color images that can be

manipulated in MATLAB. This array stores the different sub-images (in the case of the Illum, 15 x 15 sub-images resulting in 225 different perspectives). A sample of this image type is shown in Figure A.2, which was imaged using the lens configuration in Figure A.1. The highest exposed image is at an off-center position, likely due to a misalignment in the multi lens system. There are also instances of image formation at six corners, likely from the hexagonal configuration of the microlens array in the Lytro Illum. A sample image from the array shown in Figure A.2 that is offset from the center is shown in Figure A.3.

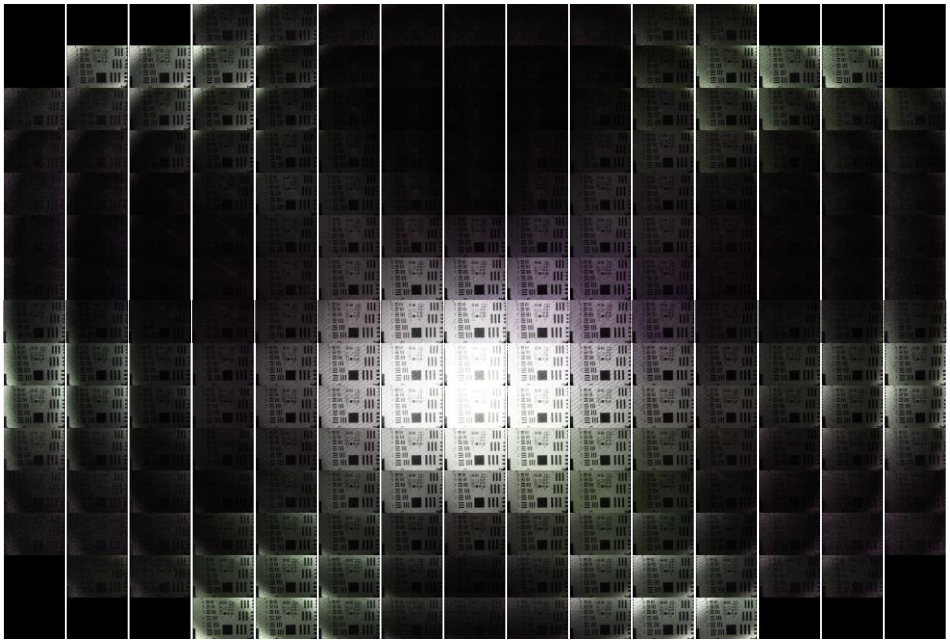

Figure A.2: The 225 different perspectives for imaging a USAF test chart. The array of 225 images (15 x 15) are 625x434px.

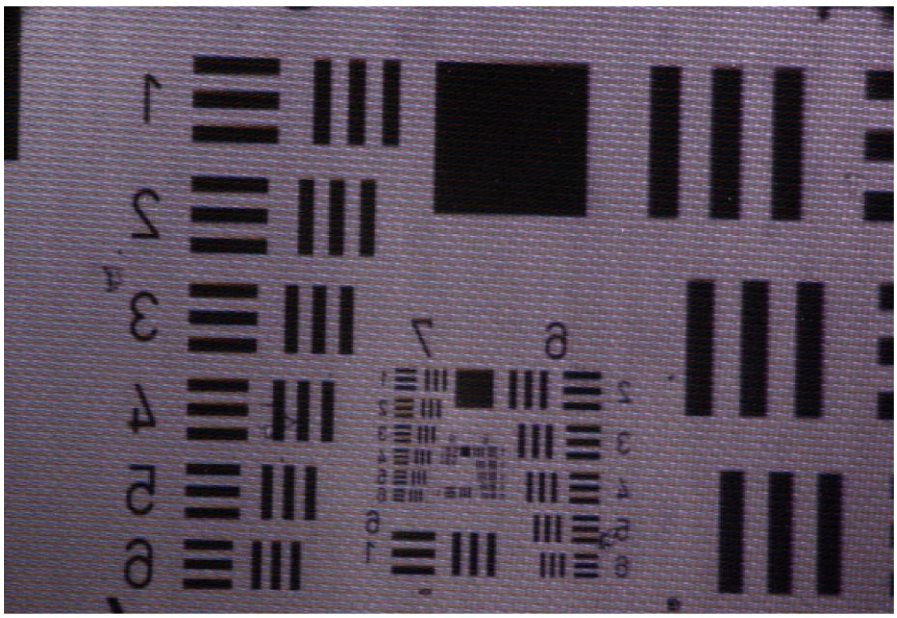

Figure A.3: USAF test chart image with the Lytro Illum and the lens configuration shown in Figure A.1. The smallest resolvable bars are on the order of 2 microns.

The Plenoptic imaging system was then used to image the ECN Spray D injector. A sample light field image of a spray is shown in Figure A.4. The decrease in image quality with radial distance from the center is from the vignette effect and the ballistic light. An image radially offset by one location from the center is shown in Figure A.5. The lower image resolution (640 x 480 pixels) and change in effective magnification make this image nyquist limited. The image processing algorithm produces a seemingly checkerboard appearance on the figure, with problematic pixel "hot spots" seen in Figure A.4.

Despite the numerous areas for improvement in this setup, a high speed Plenoptic microscopy system has been demonstrated with a single shot image and with a Color-Coded Pulse-Burst Microscopy image (not shown) for the first time. Some areas for improvement with the Plenoptic system are as follows.

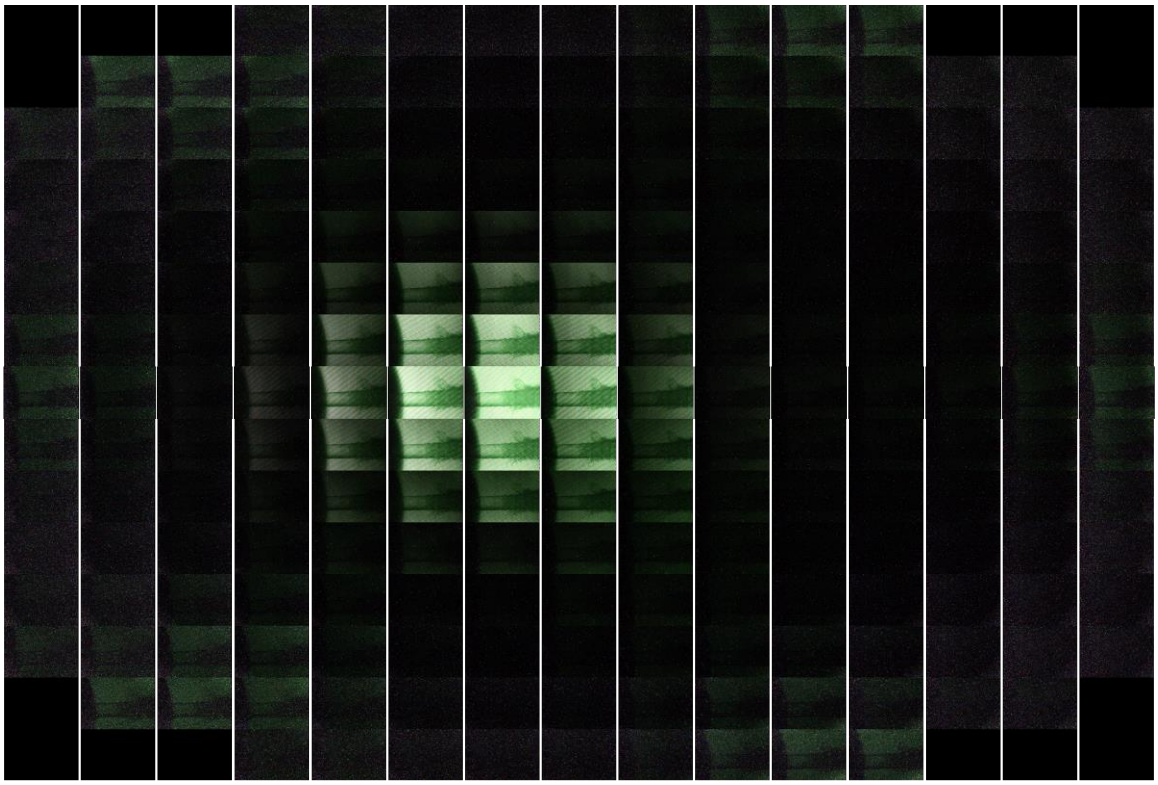

Figure A.4: Light field image of a spray at 400 bar fuel injection, in the transient regime of the spray

The vignette effect on the light field and lack of angular resolution (few images in the light field are properly exposed) are due to a mismatch of aperture throughout the four lens system. To resolve this, a wider main lens and microscopic objective will be needed. The relatively low F number of the infinity main body and the entrance pupil diameter to the objective are the two causes of this effect. The custom F/2.8 lens detailed earlier would be a potential remedy for this.

Further improvement could be made to the light field camera by using a different microlens array and relay lens. Other work [61], [62] has demonstrated this possibility. The microlens pitch in the Lytro Illum is $14\,\mu m$, and pixel pitch is $0.89\,\mu m/px$, so 225 (15 x 15) effective perspectives are obtained from each microlens. Scientific grade

microlens assemblies are available from Thorlabs and other optics suppliers but have pitches on the order of 100 μm for the microlenses, which depending on the post processing algorithm would either have more low resolution sub images, or have fewer high resolution sub images.

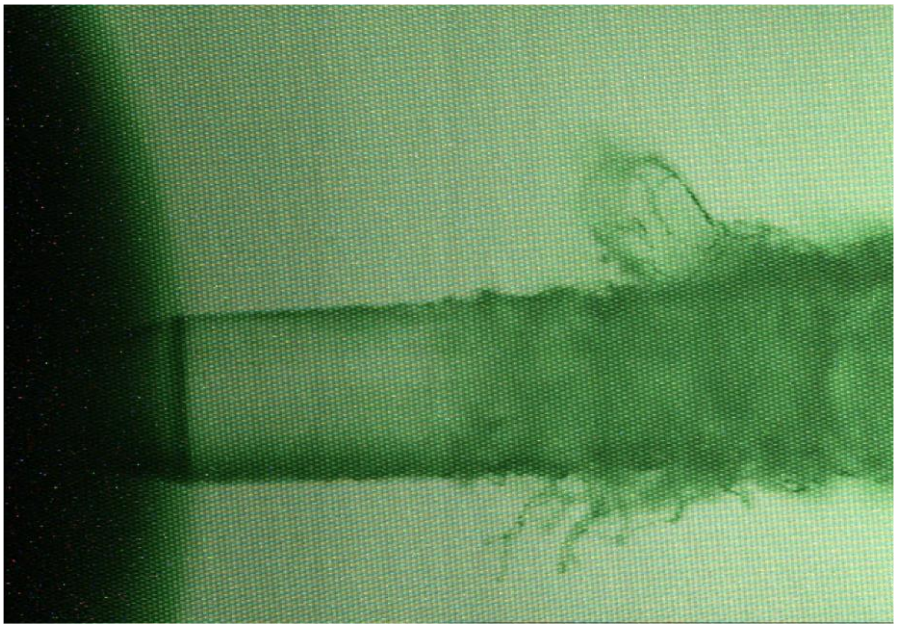

Figure A.5: Single shot image from the light shown in Figure A.4. Image resolution is 625 x 434 px.

REFERENCES

[1] S. Ramachandran and U. Stimming, "Well to wheel analysis of low carbon alternatives for road traffic," *Energy Environ. Sci.*, vol. 8, no. 11, pp. 3313–3324, 2015.

[2] K. Tweed, "Smokestack vs. Tailpipe: How Clean Are Electric Vehicles?," *greentechmedia.com*, 2012. [Online]. Available: https://www.greentechmedia.com/articles/read/smokestack-vs-tailpipe-how-clean-are-electric-vehicles.

[3] A. Elgowainy *et al.*, *Well -to-Wheels Analysis of Energy Use and Greenhouse Gas Emissions of Plug-In Hybrid Electric Vehicles*. 2010.

[4] J. J. J. Louis, "Well-to-wheel energy use and greenhouse gas emissions for various vehicle technologies," *SAE Tech. Pap.*, vol. 2001, no. 724, 2001.

[5] BloombergNEF, "Electric Vehicle Outlook 2019," 2019. [Online]. Available: https://about.bnef.com/electric-vehicle-outlook/#toc-viewreport.

[6] Mazda, "SKYACTIV-X: a revolutionary new combustion engine," 2017. [Online]. Available: https://www.mazda.com/en/innovation/mazda-stories/engineers/skyactiv-x/.

[7] A. Lefebvre, *Atomization and Sprays*. 2018.

[8] B. J. Azzopardi, "Sauter Mean Diameter," *Thermopedia*, 2011. [Online]. Available: http://www.thermopedia.com/content/1108/.

[9] G. M. Faeth, "Structure and atomization properties of dense turbulent sprays," *Symp. Combust.*, vol. 23, no. 1, pp. 1345–1352, Jan. 1991.

[10] R. D. Reitz and F. V. Bracco, "Mechanism of atomization of a liquid jet," *Phys. Fluids*, vol. 25, no. 10, p. 1730, 1982.

[11] P.-K. Wu and G. M. Faeth, "Aerodynamic Effects on Primary Breakup of Turbulent Liquids," *At. Sprays*, vol. 3, no. 3, pp. 265–289, 1993.

[12] R. D. Reitz, "Modeling Atomization Processes in High-Pressure Vaporizing Sprays," *At. Sprays Technol.*, vol. 3, pp. 309–337, 1987.

[13] S. Som *et al.*, "Development and Validation of a Primary Breakup Model for Diesel Engine Applications," 2009.

[14] A. Kastengren *et al.*, "Measurements of droplet size in shear-driven atomization using ultra-small angle x-ray scattering," *Int. J. Multiph. Flow*, vol. 92, pp. 131–139, 2017.

[15] C. F. Powell and D. Duke, "Measurements of Diesel Spray Droplet Size with Ultra-Small Angle X-Ray Scattering Argonne National Laboratory Argonne , IL 60439 USA A . L . Kastengren *, J . Ilavsky X-Ray Science Division , Advanced Photon Source Argonne National Laboratory," no. May, 2013.

[16] H. Zaheer, “Transient Microscopy of Primary Atomization in Gasoline Direct Injection Sprays,” no. May, 2015.

[17] Y. Kim, “Development of Spectral Microscopy Imaging Technique for Time-Resolved Imaging of Primary Breakup in High-Pressure Fuel Sprays,” no. December, 2013.

[18] C. Crua, M. R. Heikal, and M. R. Gold, “Microscopic imaging of the initial stage of diesel spray formation,” *Fuel*, vol. 157, pp. 140–150, Oct. 2015.

[19] V. Kirsch, M. A. Reddemann, J. Palmer, and R. Kneer, “Zooming into primary breakup mechanisms of high-pressure automotive sprays,” *Pap. Present. ILASS–Europe 2017*, no. September 6-8, 2017.

[20] Z. Feng, C. Tang, Y. Yin, P. Zhang, and Z. Huang, “Time-resolved droplet size and velocity distributions in a dilute region of a high-pressure pulsed diesel spray,” *Int. J. Heat Mass Transf.*, vol. 133, pp. 745–755, 2019.

[21] A. A. Aguirre-Pablo, M. K. Alarfaj, E. Q. Li, J. F. Hernández-Sánchez, and S. T. Thoroddsen, “Tomographic Particle Image Velocimetry using Smartphones and Colored Shadows,” *Sci. Rep.*, vol. 7, no. 1, pp. 1–18, 2017.

[22] T. J. McGregor, D. J. Spence, and D. W. Coutts, “Laser-based volumetric flow visualization by digital color imaging of a spectrally coded volume,” *Rev. Sci. Instrum.*, vol. 79, no. 1, 2008.

[23] S. Funatani, T. Takeda, and K. Toriyama, “High-Resolution Three-Color Piv Technique Using a Digital Slr Camera,” *J. Flow Vis. Image Process.*, vol. 20, no. 1–2, pp. 35–45, 2014.

[24] J. S. Silfies, S. . A. Schwartz, and M. W. Davidson, “The Diffraction Barrier in Optical Microscopy.” [Online]. Available: https://www.microscopyu.com/techniques/super-resolution/the-diffraction-barrier-in-optical-microscopy.

[25] ISO, “ISO 12233:2017, Photography - Electronic Still Picture Imaging - Resolution And Spatial Frequency Responses,” *International Organization for Standardization*, 2017.

[26] N. T. Clemens, “Flow Imaging,” *Encycl. Imaging Sci. Technol.*, pp. 390–419, 2002.

[27] Edmond Optics, “Understanding Focal Length and Field of View.” [Online]. Available: https://www.edmundoptics.com/resources/application-notes/imaging/understanding-focal-length-and-field-of-view/.

[28] C. Genzale, “2014 ARO Project Proposal,” pp. v–xx, 2013.

[29] J. Menser, F. Schneider, T. Dreier, and S. A. Kaiser, “Multi-pulse shadowgraphic RGB illumination and detection for flow tracking,” *Exp. Fluids*, vol. 59, no. 6, pp. 1–11, 2018.

[30] H. Purwar *et al.*, “Ultrafast high-repetition imaging of fuel sprays using picosecond fiber laser,” *Opt. Express*, vol. 23, no. 26, p. 33396, 2015.

[31] Company 7, “QUESTAR QM-1 PHOTO-VISUAL LONG DISTANCE

MICROSCOPE," 2000. [Online]. Available: http://www.company7.com/questar/microscope/qm1.html.

[32] I. P.-O. Company, "Model K2 DistaMax Long-Distance Microscope System," 2017. .

[33] B. Jähne, "Practical handbook on image processing for scientific and technical applications," *Choice Rev. Online*, vol. 42, no. 02, pp. 42-0986-42–0986, 2013.

[34] S. Eddins, "Tips for reading a camera raw file into MATLAB," 2011. [Online]. Available: https://blogs.mathworks.com/steve/2011/03/08/tips-for-reading-a-camera-raw-file-into-matlab/.

[35] H. S. Malvar, Li-wei He, and R. Cutler, "High-quality linear interpolation for demosaicing of Bayer-patterned color images," *2004 IEEE Int. Conf. Acoust. Speech, Signal Process.*, vol. 3, pp. iii-485–8, 2004.

[36] L. Goss, J. Estevadeordal, and J. Crafton, "Kilo-Hertz Color Particle Shadow Velocimetry (PSV)," in *37th AIAA Fluid Dynamics Conference and Exhibit 25 - 28 June 2007, Miami, FL AIAA*, 2012, no. June, pp. 1–11.

[37] J. Jiang, D. Liu, J. Gu, and S. Susstrunk, "What is the space of spectral sensitivity functions for digital color cameras?," *Proc. IEEE Work. Appl. Comput. Vis.*, pp. 168–179, 2013.

[38] Luxottica, "Absorption and Emisison Spectra of Dyes." 2019.

[39] J. Menser, T. Dreier, S. Kaiser, and C. Schulz, "Multi-pulse RGB illumination and detection for particle tracking velocimetry," *7th Eur. Combust. Meet.*, pp. 1–6, 2015.

[40] S.-Y. Jaw, J.-J. Sheen, and R. Hwang, "DEVELOPMENT AND APPLICATION OF AN ALTERNATING-COLOR MICRO-PIV SYSTEM Shenq-Yuh," in *ASME 2014 International Mechanical Engineering Congress and Exposition*, 2014, pp. 1–8.

[41] LightSpeed Technologies, "HPLS-36 Series Single Emitter with Built in Driver," 2018. [Online]. Available: http://www.light-speed-tech.com/hpls-36-3-2/.

[42] RP Photonics, "Speckle," *RP Photonics Encyclopedia*. [Online]. Available: https://www.rp-photonics.com/speckle.html.

[43] B. Knox and C. Genzale, "Effects of End-of-Injection Transients on Combustion Recession in Diesel Sprays," *SAE Int. J. Engines*, vol. 9, no. 2, pp. 932–949, 2016.

[44] Sandia National Labs, "Engine Combustion Network | Spray D Nozzle Geometry," 2018. [Online]. Available: https://ecn.sandia.gov/diesel-spray-combustion/target-condition/spray-d-nozzle-geometry/. [Accessed: 16-Apr-2019].

[45] R. D. Reitz, "Atomization and other Breakup Reigmes of a Liquid Jet.pdf." 1978.

[46] V. Kirsch *et al.*, "Transparent high-pressure nozzles for visualization of nozzle internal and external flow phenomena," *Rev. Sci. Instrum.*, vol. 90, no. 3, 2019.

[47] J. Shinjo and A. Umemura, "Simulation of liquid jet primary breakup: Dynamics of ligament and droplet formation," *Int. J. Multiph. Flow*, vol. 36, no. 7, pp. 513–532, 2010.

[48] L. M. Pickett, J. Manin, A. Kastengren, and C. Powell, “Comparison of Near-Field Structure and Growth of a Diesel Spray Using Light-Based Optical Microscopy and X-Ray Radiography,” *SAE Int. J. Engines*, vol. 7, no. 2, pp. 1044–1053, 2014.

[49] J. Yon, J.-B. Blaisot, and M. Ledoux, “Unusual Laser-Sheet Tomography Coupled With Backlight Imaging Configurations To Study the Diesel Jet Structure At the Nozzle Outlet for High Injection Pressures,” *J. Flow Vis. Image Process.*, vol. 9, no. 1, p. 19, 2014.

[50] B. Chehroudi, S. H. Chen, F. V. Bracco, and Y. Onuma, “On the intact core of full-cone sprays,” *SAE Tech. Pap.*, no. July, 1985.

[51] J. W. Hoyt and J. J. Taylor, “Waves on water jets,” *J. Fluid Mech.*, vol. 83, no. 1, pp. 119–127, 1977.

[52] R. D. Reitz, “Computer modeling of Sprays, in: Spray Technology Short Course,” 1996.

[53] J. Manin, A. Kastengren, and R. Payri, “Understanding the acoustic oscillations observed in the injection rate of a common-rail direct injection diesel injector,” *J. Eng. Gas Turbines Power*, vol. 134, no. 12, pp. 1–10, 2012.

[54] G. M. Magnotti *et al.*, “Modeling the Influence of Nozzle-Generated Turbulence on Diesel Sprays Woodruff School of Mechanical Engineering , Georgia Institute of Technology , Atlanta , GA Energy Systems Division , Argonne National Laboratory , Lemont , IL 60439 X-Ray Science Divis,” no. May, 2017.

[55] P.-K. Wu, L.-K. Tseng, and G. M. Faeth, “Primary Breakup in Gas / Liquid Mixing Layers for Turbulent Liquids,” *Aiaa*, vol. 30, p. 12, 1992.

[56] J. O. Hinze, “Fundamentals of the hydrodynamic mechanism of splitting in dispersion processes,” *AIChE J.*, vol. 1, no. 3, pp. 289–295, 1955.

[57] P. M. Hubel, J. Liu, and R. J. Guttosch, “Spatial frequency response of color image sensors: Bayer color filters and Foveon X3,” *Sensors Camera Syst. Sci. Ind. Digit. Photogr. Appl. V*, vol. 5301, no. May, p. 402, 2004.

[58] R. J. Guttosch, “Investigation of Color Aliasing of High Spatial Frequencies and Edges for Bayer-Pattern Sensors and Foveon X3 ® Direct Image Sensors,” *Foveon Inc*, pp. 1–8, 2002.

[59] F. Guo, Y. Yang, B. Chen, and L. Guo, “A novel multi-scale edge detection technique based on wavelet analysis with application in multiphase flows,” *Powder Technol.*, 2010.

[60] R. Ng *et al.*, “Light Field Photography with a Hand-held Plenoptic Camera,” *Main*, pp. 1–11, 2005.

[61] M. Levoy, R. Ng, A. Adams, M. Footer, and M. Horowitz, “Light field microscopy,” *ACM SIGGRAPH 2006 Pap. - SIGGRAPH ’06*, p. 924, 2006.

[62] L. Mignard-debise, I. Ihrke, L. Mignard-debise, I. Ihrke, L. Microscopy, and L. Mignard-debise, “Light-field Microscopy with a Consumer Light-field Camera,” 2015.

[63] D. Dansereau, “Light Field Toolbox v0.4,” *MathWorks File Exchange*, 2015. [Online]. Available: https://www.mathworks.com/matlabcentral/fileexchange/49683-light-field-toolbox-v0-4.